Astronomically controlled aridity in the Sahara since at least 11 million years ago

Anya J. Crocker[1,2,*], B. David A. Naafs[3], Thomas Westerhold[4], Rachael H. James[1], Matthew J. Cooper[1], Ursula Röhl[4], Richard D. Pancost[3], Chuang Xuan[1], Colin P. Osborne[2], David J. Beerling[2], Paul A. Wilson[1]

[1]University of Southampton, Waterfront Campus, National Oceanography Centre Southampton, SO14 3ZH, United Kingdom.

[2]Department of Animal and Plant Sciences, University of Sheffield, Sheffield, S10 2TN, United Kingdom.

[3]Organic Geochemistry Unit, School of Chemistry, School of Earth Sciences, and Cabot Institute for the Environment, University of Bristol, Bristol, United Kingdom.

[4]MARUM – Center for Marine Environmental Sciences, University of Bremen, Leobener Strasse, 28359 Bremen, Germany.

* Correspondence to: anya.crocker@noc.soton.ac.uk

Abstract

The Sahara is the largest hot desert on Earth. Yet, the timing of its inception and its response to climatic forcing is debated, leading to uncertainty over the causes and consequences of regional aridity. Here we present detailed records of terrestrial inputs from Africa to North Atlantic deep-sea sediments, documenting a long and sustained history of astronomically-paced oscillations between a humid and arid Sahara from over 11 million years (Myr) ago. We show that intervals of strong dust emissions from the heart of the continent predate both the intensification of northern hemisphere glaciation and the oldest land-based evidence for a Saharan Desert by millions of years. We find no simple long-term gradational transition towards an increasingly arid climate state in northern Africa, suggesting that aridity was not the primary driver of gradual Neogene expansion of African savanna C_4 grasslands. Instead, insolation-driven wet-dry shifts in Saharan climate were common over the last 11 Myr and we identify three distinct stages in the sensitivity of this relationship. Our data provide context for evolutionary outcomes on Africa, for example, we find that astronomically-paced arid intervals predate the oldest fossil evidence of hominid bipedalism by at least 4 Myr.

Main text

Prominent from space, the Saharan desert is a vast, bare, intensely arid, dust-exporting landscape that grew 10% in response to climatic forcing during the 20th century[1]. A recognisable Saharan desert is widely suggested to originate in the late Pliocene, ~2.6 Myr ago, coupled to the development of major continental ice sheets in the Northern

Hemisphere and their expansion during the mid-Pleistocene transition (ca. 1.2–0.6 Myr ago)[2,3]. Yet, this interpretation has been challenged[4], and evidence of Saharan dust in ~4.8 Myr old Canary Island palaeosols[5] and proposed aeolian dune deposits from the Djurab of Chad dated to ~7 Myr ago[6] hint at an earlier inception of desert conditions. Weakening of the summer monsoon in climate model simulations of the response to Tethys Sea closure is hypothesized[7] to account for earlier desertification. However, the significance of the fossil dunes is highly controversial[8], estimated dates of Tethys closure span more than 20 Myr[9,10] and existing climate records are too sparse to test these competing hypotheses for desert inception. Thus, the geological history of the world's largest hot desert, which exerts a major influence on the Earth's energy balance and global biogeochemical cycles, remains poorly constrained.

Unearthing terrestrial climate history in marine sediments

We investigated the evolution of African aridity and atmospheric dust export over the last 11 Myr by developing continuous, high resolution and well-dated geochemical records of terrigenous inputs from northern Africa to marine sediment archives. We studied Ocean Drilling Project (ODP) Site 659 off Mauritania (Supplementary Figure 1), situated underneath the main modern Saharan dust plume. Pronounced cycles in colour and lithology of Site 659 sediments record changes in terrigenous content and, in the seminal study of Tiedemann et al.[11], these changes were quantified and used to infer dust inputs and aridity change on Africa over the past 5 million years. Yet, that hydroclimate reconstruction is now called into question for three reasons: First, distal, fine-grained material, likely of riverine origin, also contributes to the lithogenic fraction of sediment accumulating on the northwest African margin including Site

659[12,13] (see Supplementary Information). Second, the proportion of terrigenous material in marine sediments is also influenced by marine carbonate deposition and dissolution, which may exert a significant control, particularly in Pliocene and Miocene-aged sediments at Site 659[14,15]. Third, dust supply to the atmosphere and marine sediments is controlled not only by aridity but also wind strength[16].

We used X-ray fluorescence (XRF) core scanning to both document dust accumulation in the North Atlantic Ocean and infer African hydroclimate over the last 11 Myrs geochemically (Figure 1). Because dust flux estimates show a strong wind strength dependence and can be biased by carbonate dissolution and rapid fluctuations in sediment accumulation[15], we use two geochemical ratios, [Al+Fe]/[Si+K+Ti] and ln[Zr/Rb], to reconstruct hydroclimate variability. High [Al+Fe]/[Si+K+Ti] values are associated with low inputs of Si-rich dust and more intense chemical weathering under humid climates[17] while high ln[Zr/Rb] values indicate dominance of coarse dust over fine river clays[12]. Crucially, these two ratios employ only lithophile elements and so, unlike dust fluxes, they are independent of sea-floor carbonate dissolution and dilution and show strong agreement with hydroclimate reconstructions based upon deuterium isotopic signatures of plant waxes (Figure 2, Extended Data Figures 1–2 and Supplementary Information). Our dust flux reconstructions are similar to thorium-normalization based estimates from nearby site MD03-2705[15] (Extended Data Figure 3 and Supplementary Information) suggesting that, although the influence of dilution, dissolution, rapid sedimentation rate fluctuations and sediment remobilisation cannot be entirely ruled out, they are not likely main drivers of reconstructed dust fluxes at Site 659.

89 Our high-resolution records (Figure 1) reveal a long history of repeated dramatic
90 shifts in hydroclimate between dry dusty conditions and more humid intervals
91 reaching back 11 Myrs. The most recent of these is the African Humid Period (AHP1)
92 in the early Holocene, when the Saharan landscape was well-vegetated and cross-cut
93 by a network of rivers and lakes[13, 18-20] with abundant archaeological sites, some
94 adorned with rock art depictions of giraffe, elephant, hippopotamus and domesticated
95 cattle[21]. Throughout our record, dark terrigenous-rich sediment layers at Site 659 have
96 significantly higher ln[Zr/Rb] and lower [Al+Fe]/[Si+K+Ti] values than pale layers
97 indicating that they contain a greater proportion of coarser grains, and have a
98 chemical signature approaching dust end-member values (Figure 3, Extended Data
99 Figure 4 and Supplementary Information). Thus, the dark layers consistently signify
100 high dust deposition linked to aridity over northern Africa rather than high riverine
101 sediment input or merely strong sea floor carbonate dissolution. Intervening paler
102 layers consistently record low ln[Zr/Rb] and high [Al+Fe]/[Si+K+Ti], indicating far
103 less dusty conditions on Africa. Spectral analysis reveals that this climatic variability
104 is primarily paced by precession and obliquity, with a strong signature of eccentricity
105 only documented in the oldest (Miocene) part of our records (Extended Data Figures
106 5–6 and Supplementary Information).

107

108 Long-lived pulsing of Saharan dust export

109 We identify three distinct stages in the evolution of Saharan hydroclimate state over
110 the past 11 Myrs, separated by transitions with statistically significant shifts in central
111 tendency and dispersion in our datasets (Figure 1, Extended Data Figure 7 and
112 Supplementary Information). Stage I (>6.9 Myr ago) reveals astronomically-paced

development of arid and dust-producing regions on Africa from at least 11 Myr ago. Pronounced dark sediment layers consistently show high ln[Zr/Rb] and low [Al+Fe]/[Si+K+Ti] values, confirming that these layers are, like those in the younger part of the record, associated with aridity (Figure 3, Extended Data Figure 4). Both ln[Zr/Rb] and [Al+Fe]/[Si+K+Ti] values suggest that African climate was more arid during the Late Miocene than the Pliocene, however estimated dust flux maxima are lower. Given the importance of deflation-promoting high wind speeds (gustiness) in dust transport, we attribute this result to warmer Miocene high latitudes weakening latitudinal temperature gradients (Figure 1c), resulting in lower wind speeds and less effective deflation and dust transport[22-25]. Nevertheless, our records document substantial dust emissions that predate the oldest land-based evidence (~7 Myr ago) for Miocene initiation of northern African hyperaridity[6] by at least 4 Myr, and predate Late Pliocene intensification of Northern Hemisphere Glaciation (iNHG)[2, 3] by at least 8 Myr.

A shift towards increased [Al+Fe]/[Si+K+Ti] values followed by decreased ln[Zr/Rb] from ~6.9 Ma marks the transition into stage II (which covers the latest Miocene to the late Pliocene, ~5.75–3.5 Ma), indicating wetter conditions with more fine-grained sedimentary inputs (Figure 1f and g). Increasing variability in [Al+Fe]/[Si+K+Ti], ln[Zr/Rb] and dust fluxes is also recorded implying a heightened sensitivity of northern African humidity to astronomical forcing, although cycle amplitudes may also be more attenuated by bioturbation in Stage I where sedimentation rates are lower (Supplementary Figure 2). Dust fluxes during stage II are lower during humid events associated with insolation maxima but higher during arid insolation minima than seen for equivalent forcing in stage I. We attribute this result to the development

of extensive Pliocene river systems and lakes (including Lake Chad which has a Latest Miocene origin[26]) during 'wet orbits' that, once desiccated, became dust-producing hot-spots[27,28] during succeeding 'dry orbits'.

The transition to Stage III, which covers the last ~2.25 Myrs (early Pleistocene to Recent) of African climate history, is characterized by a shift towards more arid conditions (decreasing [Al+Fe]/[Si+K+Ti] centred around 3.1 Ma) followed, ca. 400 kyr later, by increased mean values of ln[Zr/Rb] and dust fluxes (which also show higher amplitude variability), closely contemporaneous with the intensification of glacials as revealed by benthic oxygen isotope records[29] (Figure 1b). The highest dust fluxes in our records during Stage III are consistent with the suggestion that the growth of large continental ice sheets in the Northern Hemisphere promoted the development of more arid and dusty conditions on Africa through steepening latitudinal temperature gradients and strengthening winds[3,30].

Consistency of source

We investigated the source of terrigenous material accumulating at ODP Site 659 over the last 11 Myr using radiogenic isotopes. Today, dust is generated widely across three geochemically distinct northern African preferential source areas (PSAs)[31]. Strontium and neodymium isotopic signatures of the lithogenic fraction of Site 659 sediments are remarkably consistent compared to the range in modern PSA signatures and lie between those reported for the Central and currently undersampled Western source regions[31] (Figure 4). These results imply that the terrigenous source regions remained broadly unchanged over the past 11 Myr and that variability in grain size is

not a major control on our data (Extended Data Figures 8–10 and Supplementary Information). This observation, together with the high ln[Zr/Rb] and [Al+Fe]/[Si+K+Ti] values recorded during Miocene insolation minima, indicates that dust-producing regions existed in the inland Sahara region and were activated by astronomical forcing back to at least 11 Myr ago. We conclude that while iNHG in the late Pliocene (~3.3–2.5 Myr ago) drove increased dust fluxes (Figure 1h), it was not responsible for the inception of the Saharan desert.

Rainfall climate, C_4 savannas and evolutionary outcomes

Savannas dominated by C_4 grasses expanded extensively during the late Miocene[32,33], but the cause of this major reorganization of the terrestrial biosphere is controversial. Both aridification and decreasing pCO_2 are proposed drivers of this grassland ecosystem shift, aided by strong positive feedbacks associated with fire, and regionally modified by latitude, altitude and rainfall seasonality[32-37]. To better understand the potential role of hydroclimate variability in driving the expansion of C_4 grasslands, we compare our geochemical datasets to stable carbon ($\delta^{13}C$) and hydrogen (δD) isotope signatures of leaf wax long-chain *n*-alkanes at Site 659 (Figures 1d and 2). The carbon isotope signature of plant waxes is strongly controlled by the photosynthetic pathway of the parent plant: *n*-alkanes from C_4 plants are isotopically heavier (–21.4±2.2 ‰) than C_3 plants (–34.9±2.7 ‰)[38].

We find little similarity between the gradational expansion of C_4 grasses in northern Africa and long-term hydroclimate trends (Figure 1). The plant wax records integrate material from across a large source area that was dominated by C_4 vegetation during

186 the Quaternary[39,40], potentially contributing to the expression of only modest change
187 in *n*-alkane $\delta^{13}C$ in response to insolation forcing in the youngest part of the record.
188 Nevertheless, the hydroclimate signal in North Africa ([Al+Fe]/Si+K+Ti], ln[Zr/Rb]
189 and *n*-alkane δD[36,39,40]) is dominated by astronomical variability, while the vegetation
190 signal (*n*-alkane $\delta^{13}C$[36,39,40]) is dominated by the gradual long-term trend that defines
191 the C_3-C_4 transition and is not replicated by the hydroclimate reconstructions (Figures
192 1 and 2, Supplementary Figure 3). Therefore, we find that a simple hydroclimate
193 driver cannot explain C_4 grassland expansion in northwest Africa through the
194 Neogene. A similar conclusion was reached by ref. 36. However, while that study
195 ruled out a hydroclimate control because of little inferred change in regional rainfall,
196 we document major changes in hydroclimate unaccompanied by a strong response in
197 C_4 plant dominance (Figure 2). This decoupling between aridity and C_3-C_4
198 composition does not rule out an influence of aridity on C_4 vegetation dominance, but
199 suggests that the relationship was not simple. An improved record of Neogene pCO_2
200 variability (Figure 1a) is needed to better understand coupling between global climate
201 state, hydroclimate and the rise of C_4 grasslands.

202

203 An inferred progressive aridification of Africa and spread of savanna ecosystems has
204 been linked to speciation and development of long-range mobility in hominins[3, 41] and
205 extinction of many large mammals[32,42]. Our long, detailed, continuous marine records
206 help to develop the environmental framework needed to assess these evolutionary
207 outcomes on land, including the hypothesized relationships between habitat instability
208 and development in hominins of characteristics that promote adaptability[43,44]. We
209 highlight the longevity and primacy of the astronomical signal in controlling
210 hydroclimate in northern Africa. Our findings of three distinct phases in North

African hydroclimate, including relatively dry conditions during the warm Miocene, suggest no simple escalation in aridity through the late Cenozoic associated with global cooling, and argue against aridity as the primary driver of C_4 grassland expansion. Our records show evidence of changes in mean state and/or amplitude of variability in hydroclimate close to the oldest suggested fossil evidence of hominin bipedalism[45] and the earliest records of the genus *Homo*[46] (Figure 1). However, the confidence interval on the origination of the principal taxa, especially suggested bipeds, is large, implying earlier emergence[47]. New fossil finds will inevitably revise the hominin chronology, enabling a stronger understanding of the evolutionary link to climate. Meanwhile, our study reveals astronomically-paced dry and dusty conditions on Africa long before both the oldest land-based evidence of a Saharan desert and the intensification of Northern Hemisphere glaciation.

Acknowledgments

This research was funded through ERC advanced grant CDREG no. 322998 (D.J.B.) and the Royal Society Challenge Grant CHG\R1\170054 (P.A.W.) and Wolfson Merit Award WM140011 (P.A.W.). Additional funding came from University of Southampton's GCRF strategic development fund grant 519016 (P.A.W. and A.J.C.), advanced ERC grant T-GRES ref. 340923 (B.D.A.N. and R.D.P.) and a Royal Society Tata University Research Fellowship (B.D.A.N.). We thank the Natural Environment Research Council for partial funding of the mass spectrometry facilities at the University of Bristol (contract no. R8/H10/63). Financial support was also received from the Deutsche Forschungsgemeinschaft (DFG) (U.R. and T.W.) including project 242225091 (T.W).

This research used samples provided by (I)ODP, which was sponsored by the US National Science Foundation and participating countries under management of Joint Oceanographic Institutions, Inc. We thank Walter Hale, Holger Kuhlman and Alex Wülbers of the Bremen Core Repository, and Rachael Kretsis James, Andrew McCombie and Cat Evans for laboratory assistance, Angus Calder for discrete XRF analysis and Vera Lukies for assistance with XRF core scanning. Biostratigraphic information was provided by Jan Backman and Stefan Mulitza supplied the geochemical endmember unmixing code. We thank David McGee, Jessica Tierney, Tom Ezard, Clive Gamble, Alistair Pike, Katherine Grant, Sarah Feakins, Eelco Rohling and Stefan Mulitza for discussions and feedback that helped to improve this manuscript.

Author contributions

A.J.C., P.A.W., C.P.O. and D.J.B. designed the study. A.J.C. and T.W. performed the XRF measurements and developed the age model. B.D.A.N. generated the *n*-alkane $\delta^{13}C$ data and M.J.C. and A.J.C. generated the radiogenic isotope data. A.J.C. performed the sediment endmember unmixing. A.J.C. and P.A.W. led the analysis and interpretation of results with input from all authors. A.J.C., P.A.W., D.J.B. and C.P.O. led the writing of the manuscript with contributions from all other authors.

Competing interests

The authors declare no competing interests.

Figures

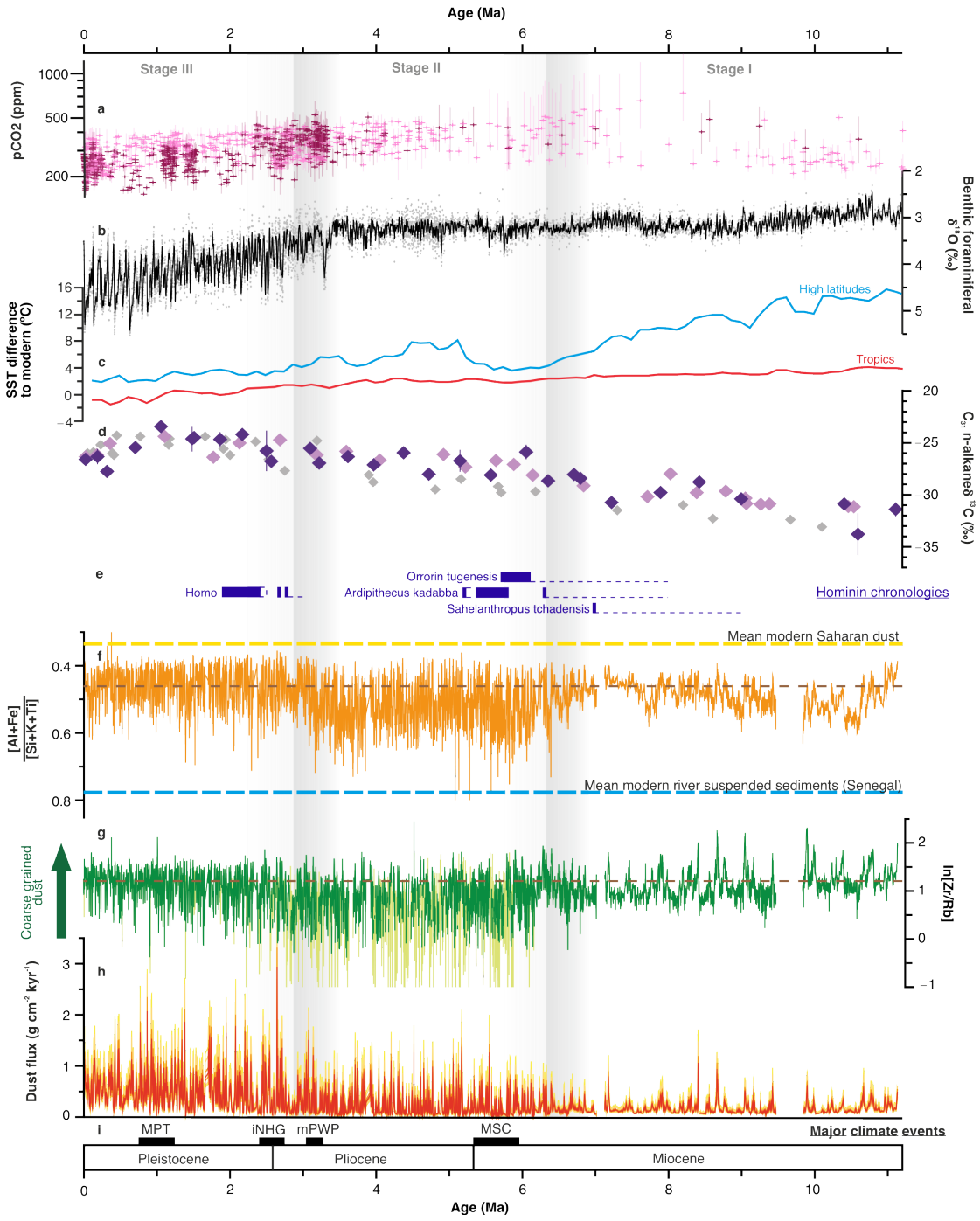

Figure 1| African hydroclimate compared to globl change over the past 11 Myr. a Atmospheric pCO_2 reconstructions (references in Supplementary Information), purple: estimates from planktonic foraminiferal boron isotopic signatures, pink: alkenone-derived estimates. **b** Cenozoic global reference benthic foraminfera oxygen

isotope dataset, with 20 kyr smoothing[29]. **c** Regional stacks of sea surface temperature difference to modern annual means[23], blue: >50°N, red: tropics. **d** $\delta^{13}C$ signature of *n*-alkanes from Site 659 (dark purple: this study, light purple: ref. 36) and offshore E. Africa[48] (grey). Error bars indicate 1σ. **e** Major events in hominid evolution. Solid bars: taxon ranges, dashed lines: confidence interval on taxon origin[47]. **f** [Al+Fe]/[Si+K+Ti] of calibrated elemental abundances. Modern endmember values updated from ref. 17 (see Supplementary Information). Dashed line marks mean over last 1 Myr. **g** ln[Zr/Rb] XRF core scan ratios. Dashed line marks mean over last 1 Myr. **h** Site 659 estimated dust flux (3pt smoothed). Median value in red; 1%, 5%, 25%, 75%, 95% and 99% percentiles also shown in shades of orange/yellow. **i** Major global climate events. MPT: mid-Pleistocene transition, iNHG: intensification of Northern Hemisphere glaciation, mPWP: mid-Pliocene warm period, MSC: Messinian Salinity Crisis. Vertical grey shading indicates transitions between climate stages.

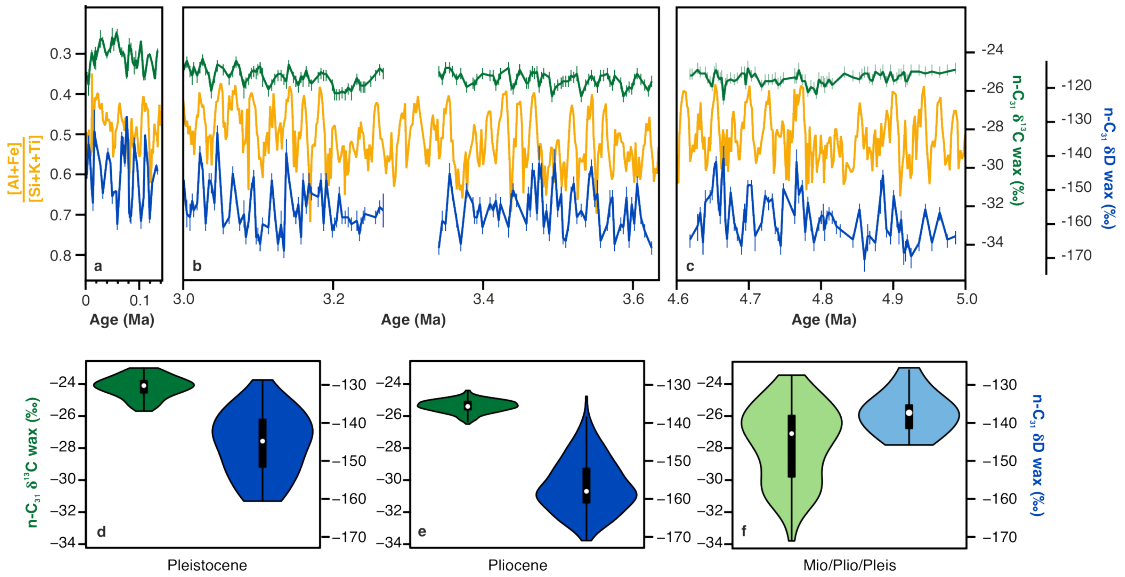

Figure 2| Relationship between lithophile element ratios and hydrogen and carbon isotopic compositions of plant waxes at Site 659. a Last glacial cycle, **b** late Pliocene, **c** early Pliocene. [Al+Fe]/[Si+K+Ti] of bulk sediment in orange (this study). Leaf wax C_{31} *n*-alkane $\delta^{13}C$ data in green[39,40] and δD in blue[39,40], error bars mark 1 standard deviation. High [Al+Fe]/[Si+K+Ti] and low *n*-alkane δD values both indicate more humid conditions. **d-f** Violin plots indicating the distribution of leaf wax C_{31} *n*-alkane $\delta^{13}C$ (green) and δD (blue**)** data in high-resolution snapshots in the Late Quaternary (**d**) and Pliocene (**e**) (data from refs. 39 and 40), and low-resolution records covering the last 11 Myr (**f,** data from this study and ref. 36). White dots indicate median values, black rectangles indicate interquartile range.

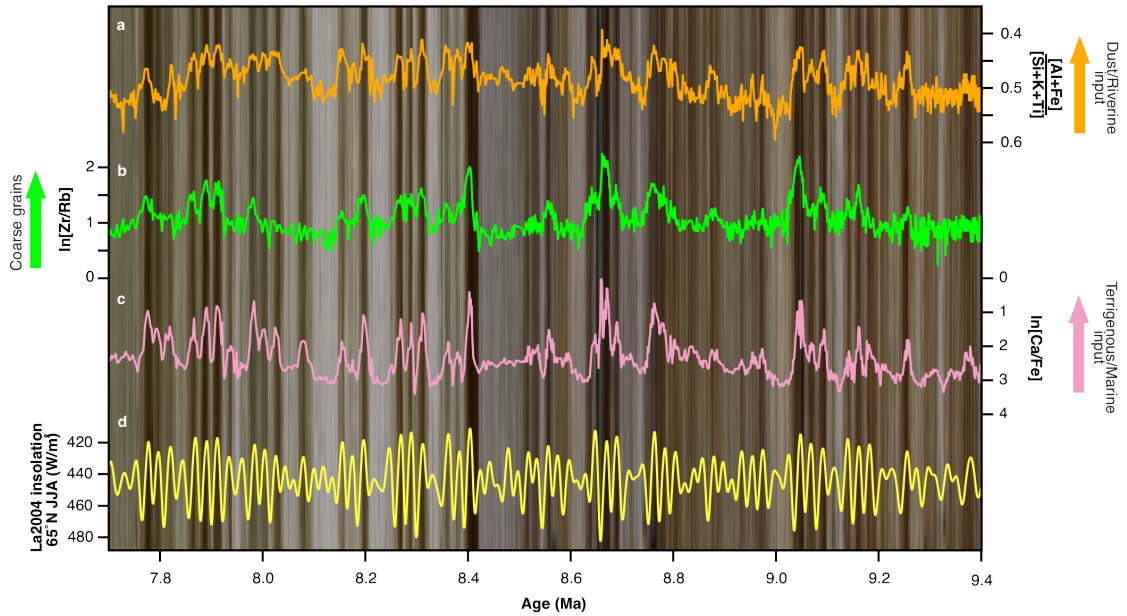

Figure 3| Strong response of African hydroclimate to astronomical forcing recorded at Site 659. Example from the late Miocene. **a** [Al+Fe]/[Si+K+Ti] of calibrated elemental abundances. **b,c** ln[Zr/Rb] and ln[Ca/Fe] XRF core scan ratios. **d** Summer insolation at 65°N[49]. Background colour shows the composited sediment core image. Darker sediments signal dry/dusty conditions, lighter sediments signal more humid intervals (see also Extended Data Figure 4 and Supplementary Information).

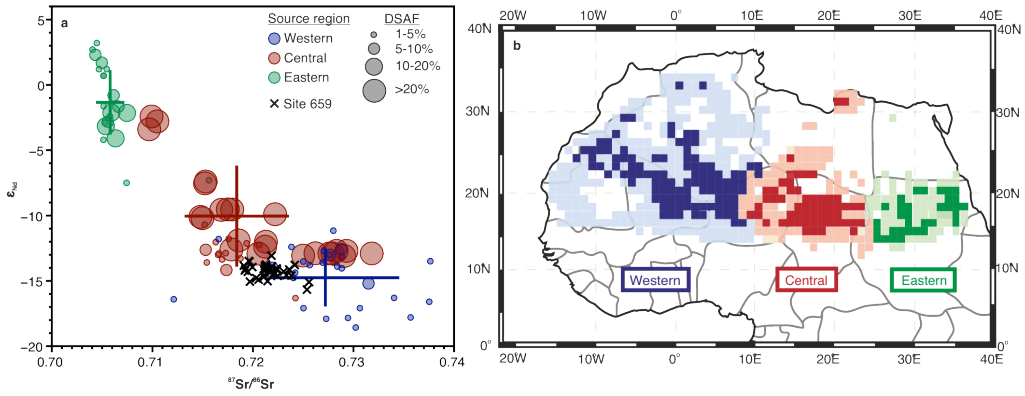

Figure 4| Radiogenic isotope signature of Site 659 lithic fraction compared to values of preferential source regions (PSAs) reveals consistent source. a Site 659 bulk sediment data (black crosses) compared to source region measurements (circles) coloured by PSA[31]. Data point size indicates dust source activation frequency (DSAF)[28]. Crosses indicate mean signatures of each PSA weighted by annual DSAF, bars denote ± one weighted standard deviation[31]. Samples for which only ε_{Nd} or $^{87}Sr/^{86}Sr$ data exist are included in the calculation of mean values but are not plotted. **b** Map of North African PSAs, adapted from ref. 31. Dust sources with activation frequencies >5% shown in bold colours, <5% in pale colours.

References

1. Thomas N, Nigam S. Twentieth-Century Climate Change over Africa: Seasonal Hydroclimate Trends and Sahara Desert Expansion. *Journal of Climate* 2018, **31**(9)**:** 3349-3370.

2. Maley J. Les changements climatiques de la fin du Tertiaire en Afrique: leur conséquence sur l'apparition du Sahara et de sa végétation. *The Sahara and the Nile* 1980**:** 63-86.

3. deMenocal PB. Plio-Pleistocene African Climate. *Science* 1995, **270**(5233)**:** 53-59.

4. Trauth MH, Larrasoaña JC, Mudelsee M. Trends, rhythms and events in Plio-Pleistocene African climate. *Quaternary Science Reviews* 2009, **28**(5–6)**:** 399-411.

5. Muhs DR, Meco J, Budahn JR, Skipp GL, Betancort JF, Lomoschitz A. The antiquity of the Sahara Desert: New evidence from the mineralogy and geochemistry of Pliocene paleosols on the Canary Islands, Spain. *Palaeogeography, Palaeoclimatology, Palaeoecology* 2019, **533:** 109245.

6. Schuster M, Duringer P, Ghienne J-F, Vignaud P, Mackaye HT, Likius A*, et al.* The Age of the Sahara Desert. *Science* 2006, **311**(5762)**:** 821.

7. Zhang Z, Ramstein G, Schuster M, Li C, Contoux C, Yan Q. Aridification of the Sahara desert caused by Tethys Sea shrinkage during the Late Miocene. *Nature* 2014, **513**(7518)**:** 401-404.

8. Kroepelin S, Swezey CS. Revisiting the Age of the Sahara Desert. *Science* 2006, **312**(5777)**:** 1138-1139.

9. McQuarrie N, van Hinsbergen DJJ. Retrodeforming the Arabia-Eurasia collision zone: Age of collision versus magnitude of continental subduction. *Geology* 2013, **41**(3)**:** 315-318.

10. Allen MB, Armstrong HA. Arabia–Eurasia collision and the forcing of mid-Cenozoic global cooling. *Palaeogeography, Palaeoclimatology, Palaeoecology* 2008, **265**(1–2)**:** 52-58.

11. Tiedemann R, Sarnthein M, Shackleton NJ. Astronomic timescale for the Pliocene Atlantic δ18O and dust flux records of Ocean Drilling Program Site 659. *Paleoceanography* 1994, **9**(4)**:** 619-638.

12. Tjallingii R, Claussen M, Stuut J-BW, Fohlmeister J, Jahn A, Bickert T*, et al.* Coherent high- and low-latitude control of the northwest African hydrological balance. *Nature Geosci* 2008, **1**(10)**:** 670-675.

13. Skonieczny C, Paillou P, Bory A, Bayon G, Biscara L, Crosta X*, et al.* African humid periods triggered the reactivation of a large river system in Western Sahara. *Nat Commun* 2015, **6**.

14. Ruddiman WF, Sarnthein M, Baldauf JG, et al. *Proc. ODP, Init. Repts., 108*. College Station, TX (Ocean Drilling Program), 1989.

15. Skonieczny C, McGee D, Winckler G, Bory A, Bradtmiller LI, Kinsley CW*, et al.* Monsoon-driven Saharan dust variability over the past 240,000 years. *Science Advances* 2019, **5**(1)**:** eaav1887.

16. McGee D, deMenocal PB, Winckler G, Stuut JBW, Bradtmiller LI. The magnitude, timing and abruptness of changes in North African dust deposition

over the last 20,000 yr. *Earth and Planetary Science Letters* 2013, **371-372:** 163-176.

17. Mulitza S, Heslop D, Pittauerova D, Fischer HW, Meyer I, Stuut J-B*, et al.* Increase in African dust flux at the onset of commercial agriculture in the Sahel region. *Nature* 2010, **466**(7303)**:** 226-228.

18. Drake NA, Blench RM, Armitage SJ, Bristow CS, White KH. Ancient watercourses and biogeography of the Sahara explain the peopling of the desert. *Proceedings of the National Academy of Sciences* 2011, **108**(2)**:** 458-462.

19. Larrasoaña JC, Roberts AP, Rohling EJ. Dynamics of green Sahara periods and their role in hominin evolution. *PloS one* 2013, **8**(10)**:** e76514.

20. Tierney JE, Pausata FSR, deMenocal PB. Rainfall regimes of the Green Sahara. *Science Advances* 2017, **3**(1).

21. Mori F. The earliest Saharan rock-engravings. *Antiquity* 1974, **48**(190)**:** 87-92.

22. McGee D, Broecker WS, Winckler G. Gustiness: The driver of glacial dustiness? *Quaternary Science Reviews* 2010, **29**(17–18)**:** 2340-2350.

23. Herbert TD, Lawrence KT, Tzanova A, Peterson LC, Caballero-Gill R, Kelly CS. Late Miocene global cooling and the rise of modern ecosystems. *Nature Geosci* 2016, **9**(11)**:** 843-847.

24. Abell JT, Winckler G, Anderson RF, Herbert TD. Poleward and weakened westerlies during Pliocene warmth. *Nature* 2021, **589**(7840)**:** 70-75.

25. Burls NJ, Fedorov AV. Wetter subtropics in a warmer world: Contrasting past and future hydrological cycles. *Proceedings of the National Academy of Sciences* 2017, **114**(49): 12888-12893.

26. Moussa A, Novello A, Lebatard A-E, Decarreau A, Fontaine C, Barboni D*, et al.* Lake Chad sedimentation and environments during the late Miocene and Pliocene: New evidence from mineralogy and chemistry of the Bol core sediments. *Journal of African Earth Sciences* 2016, **118:** 192-204.

27. Washington R, Todd M, Middleton NJ, Goudie AS. Dust‐Storm Source Areas Determined by the Total Ozone Monitoring Spectrometer and Surface Observations. *Annals of the Association of American Geographers* 2003, **93**(2)**:** 297-313.

28. Schepanski K, Tegen I, Macke A. Comparison of satellite based observations of Saharan dust source areas. *Remote Sensing of Environment* 2012, **123:** 90-97.

29. Westerhold T, Marwan N, Drury AJ, Liebrand D, Agnini C, Anagnostou E*, et al.* An astronomically dated record of Earth's climate and its predictability over the last 66 million years. *Science* 2020, **369**(6509)**:** 1383-1387.

30. Sarnthein M, Thiede J, Pflaumann U, Erlenkeuser H, Fütterer D, Koopmann B*, et al.* Atmospheric and Oceanic Circulation Patterns off Northwest Africa During the Past 25 Million Years. In: von Rad U, Hinz K, Sarnthein M, Seibold E (eds). *Geology of the Northwest African Continental Margin*. Springer Berlin Heidelberg: Berlin, Heidelberg, 1982, pp 545-604.

31. Jewell AM, Drake N, Crocker AJ, Bakker NL, Kunkelova T, Bristow CS*, et al.* Three North African dust source areas and their geochemical fingerprint. *Earth and Planetary Science Letters* 2021, **554:** 116645.

32. Cerling TE, Harris JM, MacFadden BJ, Leakey MG, Quade J, Eisenmann V*, et al.* Global vegetation change through the Miocene/Pliocene boundary. *Nature* 1997, **389**(6647)**:** 153-158.

33. Feakins SJ, Levin NE, Liddy HM, Sieracki A, Eglinton TI, Bonnefille R. Northeast African vegetation change over 12 m.y. *Geology* 2013, **41**(3): 295–298.

34. Pagani M, Freeman KH, Arthur MA. Late Miocene Atmospheric CO2 Concentrations and the Expansion of C4 Grasses. *Science* 1999, **285**(5429)**:** 876-879.

35. Beerling DJ, Osborne CP. The origin of the savanna biome. *Global Change Biology* 2006, **12**(11)**:** 2023-2031.

36. Polissar PJ, Rose C, Uno KT, Phelps SR, deMenocal P. Synchronous rise of African C4 ecosystems 10 million years ago in the absence of aridification. *Nature Geoscience* 2019, **12**(8)**:** 657-660.

37. Hoetzel S, Dupont L, Schefuß E, Rommerskirchen F, Wefer G. The role of fire in Miocene to Pliocene C4 grassland and ecosystem evolution. *Nature Geosci* 2013, **6**(12)**:** 1027-1030.

38. Naafs BDA, Hefter J, Acton G, Haug GH, Martínez-Garcia A, Pancost R*, et al.* Strengthening of North American dust sources during the late Pliocene (2.7 Ma). *Earth and Planetary Science Letters* 2012, **317–318**(0)**:** 8-19.

39. Kuechler RR, Dupont LM, Schefuß E. Hybrid insolation forcing of Pliocene monsoon dynamics in West Africa. *Climate of the Past* 2018, **14**(1)**:** 73-84.

40. Kuechler RR, Schefuß E, Beckmann B, Dupont L, Wefer G. NW African hydrology and vegetation during the Last Glacial cycle reflected in plant-wax-specific hydrogen and carbon isotopes. *Quaternary Science Reviews* 2013, **82**(0)**:** 56-67.

41. Cerling TE, Wynn JG, Andanje SA, Bird MI, Korir DK, Levin NE*, et al.* Woody cover and hominin environments in the past 6 million years. *Nature* 2011, **476**(7358)**:** 51-56.

42. Faith JT, Rowan J, Du A, Koch PL. Plio-Pleistocene decline of African megaherbivores: No evidence for ancient hominin impacts. *Science* 2018, **362**(6417)**:** 938-941.

43. Potts R. Hominin evolution in settings of strong environmental variability. *Quaternary Science Reviews* 2013, **73:** 1-13.

44. Maslin MA, Brierley CM, Milner AM, Shultz S, Trauth MH, Wilson KE. East African climate pulses and early human evolution. *Quaternary Science Reviews* 2014, **101**(0)**:** 1-17.

45. Zollikofer CPE, Ponce de León MS, Lieberman DE, Guy F, Pilbeam D, Likius A*, et al.* Virtual cranial reconstruction of Sahelanthropus tchadensis. *Nature* 2005, **434:** 755.

46. DiMaggio EN, Campisano CJ, Rowan J, Dupont-Nivet G, Deino AL, Bibi F*, et al.* Late Pliocene fossiliferous sedimentary record and the environmental context of early *Homo* from Afar, Ethiopia. *Science* 2015, **347**(6228)**:** 1355-1359.

47. Bobe R, Wood B. Estimating origination times from the early hominin fossil record. *Evolutionary Anthropology: Issues, News, and Reviews* 2021**:** 1– 11.

48. Uno KT, Polissar PJ, Jackson KE, deMenocal PB. Neogene biomarker record of vegetation change in eastern Africa. *Proceedings of the National Academy of Sciences* 2016**:** 201521267.

49. Laskar J, Robutel P, Joutel F, Gastineau M, Correia ACM, Levrard B. A long-term numerical solution for the insolation quantities of the Earth. *Astronomy & Astrophysics* 2004, **428**(1)**:** 261-285.

Methods

Site Location

ODP Site 659 is situated in the tropical North Atlantic Ocean on the Cape Verde Rise, offshore Mauritania (18.077°N 21.026°W, 3070 m water depth, for map see Supplementary Figure 1). Today, this region receives dust delivered by the trade winds during winter and spring, with additional dust transported over the site by the Saharan Air Layer predominantly during boreal summer[50-56]. The Algeria-Morocco region, Mali, Mauritania, Libya, Niger, Western Sahara and the Sahel have all been identified as regions that may currently contribute dust to the Cape Verde Islands and the surrounding ocean sediments, while evidence for a major contribution from the Bodélé depression is weaker[50-53,56-65]. The elevated position of Site 659 on the Cape Verde Rise protects it from major mass transport deposits, although grain size data reveal that multiple sites along the northwestern African margin including GeoB7920[12] and Site 659 received a significant fine-grained lithogenic component during both the Holocene and last glacial cycle that is distinct from modern dust inputs and is often attributed to a distal influence from African (palaeo)rivers[12] (Extended Data Figures 9–10 and Supplementary Information).

X-ray fluorescence

Data were collected from a total of about 275 m of drill core from three holes at ODP Site 659 using the XRF Core Scanner II (AVAATECH Serial No. 2) at MARUM - University of Bremen. Measurements were taken every 1–5 cm down core to give a consistent approximate temporal resolution of 1.5–2 kyr. Count times were 20 seconds and generator settings of 30 and 10 kV with currents of 0.75 and 0.2 mA respectively were used. The split core surface was covered with a 4 micron thin

SPEXCerti Prep Ultralene foil to avoid contamination of the XRF measurement unit and desiccation of the sediment. The data were acquired using a Canberra X-PIPS Silicon Drift Detector (SDD; Model SXD 15C-150-500) with 150eV X-ray resolution, the Canberra Digital Spectrum Analyzer DAS 1000, and an Oxford Instruments 50W XTF5011 X-Ray tube with rhodium (Rh) target material. Raw X-ray spectra were processed using an iterative least square software (WIN AXIL) package from Canberra Eurisys. Repeat runs of several core sections were used to correct for any drift in counts over time.

Ca/Fe ratios provide an indicator of the relative proportions of marine (dominated by biogenic calcium carbonate) and terrigenous (the main source of iron) sediment (Supplementary Figure 4). We use two geochemical ratios to determine the relative contribution of aeolian material to the sediment. Modern Saharan dust has much lower [Al+Fe]/[Si+K+Ti] values than samples of suspended sediment from the Senegal River (Figure 1f), the nearest and largest active river to Site 659, which drains deeply weathered lateritic tropical soils much richer in Al and Fe than the Si-rich Sahelian/Saharan dust sources[17]. We also employ Zr/Rb as an independent grain size proxy because the lithogenic dust fraction is significantly coarser than riverine-derived material on the northwest African margin[12,66], and contains a higher proportion of Zr-bearing zircon grains than Rb-rich river clays[67]. Additional geochemical ratios are shown in Supplementary Figures 5–6. Our XRF records have an average temporal resolution of approximately 2000 years.

A suite of discrete sediment samples from ODP Site 659 incorporating a wide range of lithologies were analysed by energy dispersive polarised x-ray fluorescence

555 spectrometry (EDP-XRF) at the University of St Andrews to convert the semi-
556 quantitative XRF scanner counts into concentrations (Supplementary Figure 7). The
557 downcore records plotted are calculated from ratios of these calibrated values, except
558 for ln[Zr/Rb] where counts of these trace elements are plotted.
559
560 **Stratigraphy**
561 We created a new spliced composite section for ODP Site 659 to a depth of 203.17
562 revised metres composite depth (rmcd) by correlating both the XRF core scan data
563 and core images between the three holes (A–C) drilled at Site 659, using the Code for
564 Ocean Drilling Data macros[68]. An age framework was developed from paleomagnetic,
565 nannofossil and planktonic foraminiferal datums[14,69] with ages updated to incorporate
566 more recent improvements in astrochronology[70-72]. We then correlated previously
567 published oxygen isotope values of the benthic foraminifera *Cibicides wuellerstorfi* at
568 Site 659[11] transferred onto our composite depth scale to the LR04 benthic oxygen
569 isotope stack[73] to improve age control for the youngest 5 Myr. The final age model
570 was then generating by tuning our XRF count data (ln[Ca/Fe]) to summer insolation
571 calculated at 65^{o}N in the La2004 astronomical solution[49], guided by the framework
572 provided by the biostratigraphic, magnetostratigraphic and benthic oxygen isotope
573 record. The construction of this age model is illustrated in Supplementary Figure 8. In
574 Supplementary Figure 2, we compare the age-depth relationship of our
575 astronomically-tuned age model to existing bio- and magnetostratigraphic datums.
576 Continuous wavelet power spectra[74] of both astronomically-tuned and non-
577 astronomically tuned time series data are shown in Extended Data Figure 5, with
578 results from REDFIT[75] spectral analysis shown in Extended Data Figure 6.
579

580 **Geochemical end-member unmixing**

581 Dust fluxes were estimated using an end-member unmixing approach to deconvolve
582 the relative proportions of different contributions to the bulk marine sediment, largely
583 following the method of Mulitza et al. (2010)[17]. In this approach, bulk sediment is
584 assumed to consist of three components: aeolian, riverine and marine inputs. The
585 relative abundances of Al, Si, Fe, K, Ti and Ca concentrations at Site 659 (calibrated
586 by a multivariate log calibration method[76,77] using the AvaaXelerate software[78]) were
587 compared to the chemistry of endmember compositions estimated from analyses of
588 modern sediments. The riverine endmember was constructed from ten measurements
589 of suspended sediment from the Senegal River[79], the present day catchment of which
590 stretches both north and south of Site 659. A total of 48 measurements were used to
591 construct a dust endmember, covering a wide geographical area and incorporating
592 data from dust traps, atmospheric sampling and bulk sediment from known dust
593 source areas with a range of grain sizes and local climates[59,62,80-91]. A marine
594 endmember composition of 2% Si and 98% Ca was assumed[17]. To incorporate the
595 effect of temporal changes in active terrigenous source regions and lithic fraction
596 chemistry into our dust flux estimates, a bootstrapping approach was applied. During
597 every realization, 10 of the 48 dust compositions and 4 of the 10 river compositions
598 were selected by a bootstrap with replacement routine, with the unmixing procedure
599 carried out for a total of 500 realizations of endmember compositions. Proportions of
600 aeolian and riverine endmembers were converted to fluxes using sedimentation rates
601 calculated from our composite depth scale and age model, and dry bulk sediment
602 densities estimated from shipboard measurements of gamma-ray attenuation[14] which
603 were calibrated using the discrete dry bulk density measurements of Tiedemann
604 (1991)[92]. We show that there is good agreement between our dust flux estimates and

those based on ^{230}Th normalization[15] and lithogenic %[11] in Extended Data Figures 2–3, Supplementary Figure 4 and Supplementary Information.

Lithogenic grain size measurements and geochemical data strongly support the concept of distal riverine inputs to Site 659. The proportion of the terrigenous fraction that is attributed to aeolian inputs by this geochemical unmixing approach varies strongly down core, with estimates of 0–87% dust origin. These estimates are broadly in line with those of Tjallingii et al. (2008)[12] who find that dust accounts for 5–95% of the lithic fraction through the last glacial cycle at nearby site GeoB7920 using a unmixing approach based upon grain size distributions. We cannot, however, rule out contributions to the fine-grained, high Al+Fe end-member from very fine dust or resuspended shelf material. Thus, our dust fluxes are minimum (conservative) estimates (see Supplementary Information).

Radiogenic isotopes

The Sr and Nd isotope composition of terrigenous sediments from ODP Site 659 were measured at the University of Southampton National Oceanography Centre. Approximately 1g of crushed and homogenised dried bulk sediment was decarbonated using 10 % acetic acid solution for 24 hours on a shaker table and then rinsed in deionized water. Samples were placed in a 5 % hydrogen peroxide solution for 48 hours at 65 °C to remove organic matter, then rinsed three times in deionized water. 1M $MgCl_2$ was added to the samples to remove any Sr adsorbed from seawater, which were shaken overnight then rinsed three times. A buffered hydroxylamine HCl, Na-EDTA and acetic acid solution was added to remove authigenic coatings, with samples mixed for 24 hours and then rinsed. A magnesium ion solution was added to

aid flocculation if a colloid phase formed at any stage during processing. The 'cleaned' sediments were then totally digested in concentrated nitric acid (HNO_3) and hydrofluoric acid (HF), followed by 6M HCl.

Digested sediment solutions for Sr isotope analysis were purified on columns filled with Sr-spec Resin in 3M HNO_3. Samples were loaded onto tantalum (Ta) filaments with a 1M HCl solution after a tantalum chloride (TaCl) activator solution was loaded. Isotopic measurements were made by thermal ionization mass spectrometry (Thermo-Fisher TRITON Plus). Repeated measurements of the Sr isotope standard NBS987 gave $^{87}Sr/^{86}Sr = 0.710243 \pm 0.000021$ (2σ).

Neodymium was purified from the digested sediments for isotope analysis using a standard column chemistry procedure, based upon the methods of Cohen et al. (1988)[93]. Cation exchange resin was used to strip iron and titanium from the samples, then the remaining material was then run through using Ln-Spec™ resin columns[94] to purify and concentrate neodymium. Neodymium isotope ratios were measured by multi-collector inductively coupled plasma mass spectrometry (Thermo NEPTUNE). Instrumental mass bias was corrected using the procedure of Vance and Thirlwall (2002)[95], adjusting to a $^{146}Nd/^{144}Nd$ ratio of 0.7219 and using cerium-doped standards to correct for interference of ^{142}Ce on ^{142}Nd. All ratios were normalised to the JNdi-1 standard ($^{143}Nd/^{144}Nd = 0.512115 \pm 0.000007$)[96], with independent measurements of JNdi-1 = 0.512115±0.000006 (2σ). Isotopic signatures are expressed in epsilon notation, relative to the chondritic uniform reservoir value of 0.512638[97].

Leaf wax $\delta^{13}C$

655 Compound specific stable carbon isotopes ($\delta^{13}C$) of the C_{31} and C_{33} *n*-alkane were
656 obtained from 30 samples from ODP Site 659 at the Organic Geochemistry Unit,
657 University of Bristol. For this purpose, between 5 and 10 gram of freeze-dried
658 sediment was extracted using a Microwave extraction system (Milestone Ethos Ex)
659 and a mixture of dichloromethane (DCM) and methanol (MeOH) (9:1, v/v). Fine
660 grained sediment was removed by eluting the total lipid extract (TLE) over a short (4
661 cm) inert $NaSO_4$ column using 4 ml of DCM:MeOH (9:1). The TLE was dried under
662 a gentle flow of N_2. The TLE was subsequently derivatized using pyridine and
663 BSFTA (1 hr at 70 °C) and within 24 hrs analysed on an Isoprime 100 gas
664 chromatograph combustion isotope ratio mass spectrometer (GC-C-IRMS). Samples
665 were measured in triplicate and $\delta^{13}C$ values converted to VPDB by bracketing with an
666 in-house gas (CO_2) of known $\delta^{13}C$ value. Instrument stability was monitored by
667 regular analysis of an in-house fatty acid methyl ester standard mixture and indicates
668 that long-term instrument stability was better than $\pm$ 0.3 ‰. Injection volume was 1
669 or 2 µl onto to a Zebron-I nonpolar column (50 m x 0.32 mm i.d., 0.10 µm film
670 thickness). The GC oven was programmed as: 70 °C (1 min hold) to 130 °C at 20 °C
671 min^{-1}, then to 300 °C at 4 °C min^{-1}, and a final hold at 300 °C for 25 min. Samples
672 were automatically integrated using the Ion Vantage software.
673
674 For some samples, the concentration of the C_{33} *n*-alkane was not enough to obtain a
675 reliable $\delta^{13}C$ value. The $\delta^{13}C$ of the C_{31} *n*-alkane was consistently lighter than that of
676 the C_{33} *n*-alkane from the same sample by on average 2 ‰.
677
678 **Lithogenic grain size distributions at ODP Site 659**

679 The distribution of grain sizes in lithogenic material can be used to identify different
680 terrigenous components in marine sediment. 55 samples from ODP Site 659 were
681 selected to generate grain size distribution data, incorporating a range of sediment
682 ages and lithologies. Calcium carbonate, authigenic coatings and organic matter were
683 removed following the procedure used for radiogenic isotope analysis. In addition, a
684 biogenic silica removal step was applied by sonicating samples in 1.5M NaOH.
685 Calgon was then added to the samples to prevent flocculation before analysis of the
686 lithogenic grain sizes using a Laser Coulter Sizer at the University of Southampton
687 Waterfront Campus, NOCS. The results of these grain size analyses are shown in
688 Extended Data Figure 9d.
689
690 The signatures of different terrigenous sources were separated from the bulk sediment
691 signature following the end-member modeling analysis approach (EMMA) of Dietze
692 et al. (2011)[98]. A two lithogenic end-member solution explains 88% of the variance in
693 the Site 659 data set, with the end-members shown in Extended Figure 9. The coarser
694 of these two endmembers shows a strong match with measurements of African dust
695 (Extended Data Figure 9a-b)
696

697 Data availability

698 The data presented in this study are available in the Zenodo repository (DOI:
699 10.5281/zenodo.6594643).
700

701 Methods references

702
703 50. Kumar A, Abouchami W, Galer SJG, Singh SP, Fomba KW, Prospero JM*, et*
704 *al.* Seasonal radiogenic isotopic variability of the African dust outflow to the

tropical Atlantic Ocean and across to the Caribbean. *Earth and Planetary Science Letters* 2018, **487:** 94-105.

51. Gama C, Tchepel O, Baldasano JM, Basart S, Ferreira J, Pio C*, et al.* Seasonal patterns of Saharan dust over Cape Verde – a combined approach using observations and modelling. *Tellus B: Chemical and Physical Meteorology* 2015, **67**(1)**:** 24410.

52. Patey MD, Achterberg EP, Rijkenberg MJ, Pearce R. Aerosol time-series measurements over the tropical Northeast Atlantic Ocean: Dust sources, elemental composition and mineralogy. *Marine Chemistry* 2015, **174:** 103-119.

53. Skonieczny C, Bory A, Bout-Roumazeilles V, Abouchami W, Galer SJG, Crosta X*, et al.* A three-year time series of mineral dust deposits on the West African margin: Sedimentological and geochemical signatures and implications for interpretation of marine paleo-dust records. *Earth and Planetary Science Letters* 2013, **364:** 145-156.

54. Ratmeyer V, Fischer G, Wefer G. Lithogenic particle fluxes and grain size distributions in the deep ocean off northwest Africa: Implications for seasonal changes of aeolian dust input and downward transport. *Deep Sea Research Part I: Oceanographic Research Papers* 1999, **46**(8)**:** 1289-1337.

55. Bory A, Dulac F, Moulin C, Chiapello I, Newton PP, Guelle W*, et al.* Atmospheric and oceanic dust fluxes in the northeastern tropical Atlantic Ocean: how close a coupling? *Ann Geophys* 2002, **20**(12)**:** 2067-2076.

56. Chiapello I, Bergametti G, Chatenet B, Bousquet P, Dulac F, Soares ES. Origins of African dust transported over the northeastern tropical Atlantic. *Journal of Geophysical Research: Atmospheres* 1997, **102**(D12)**:** 13701-13709.

57. Schepanski K, Tegen I, Macke A. Saharan dust transport and deposition towards the tropical northern Atlantic. *Atmos Chem Phys* 2009, **9**(4)**:** 1173-1189.

58. Caquineau S, Gaudichet A, Gomes L, Legrand M. Mineralogy of Saharan dust transported over northwestern tropical Atlantic Ocean in relation to source regions. *Journal of Geophysical Research: Atmospheres* 2002, **107**(D15)**:** AAC 4-1-AAC 4-12.

59. Formenti P, Rajot JL, Desboeufs K, Caquineau S, Chevaillier S, Nava S*, et al.* Regional variability of the composition of mineral dust from western Africa: Results from the AMMA SOP0/DABEX and DODO field campaigns. *Journal of Geophysical Research: Atmospheres* 2008, **113**(D23)**:** D00C13.

60. Friese CA, van Hateren JA, Vogt C, Fischer G, Stuut J-BW. Seasonal provenance changes in present-day Saharan dust collected in and off Mauritania. *Atmospheric Chemistry and Physics* 2017, **17**(16)**:** 10163.

61. McConnell CL, Highwood EJ, Coe H, Formenti P, Anderson B, Osborne S*, et al.* Seasonal variations of the physical and optical characteristics of Saharan dust: Results from the Dust Outflow and Deposition to the Ocean (DODO) experiment. *Journal of Geophysical Research: Atmospheres* 2008, **113**(D14).

62. Salvador P, Almeida SM, Cardoso J, Almeida-Silva M, Nunes T, Cerqueira M*, et al.* Composition and origin of PM10 in Cape Verde: Characterization of long-range transport episodes. *Atmospheric Environment* 2016, **127:** 326-339.

63. Skonieczny C, Bory A, Bout-Roumazeilles V, Abouchami W, Galer SJG, Crosta X*, et al.* The 7–13 March 2006 major Saharan outbreak: Multiproxy characterization of mineral dust deposited on the West African margin. *Journal of Geophysical Research: Atmospheres* 2011, **116**(D18).

64. Stuut J-B, Zabel M, Ratmeyer V, Helmke P, Schefuß E, Lavik G*, et al.* Provenance of present-day eolian dust collected off NW Africa. *Journal of Geophysical Research: Atmospheres* 2005, **110**(D4)**:** D04202.

65. Zhao W, Balsam W, Williams E, Long X, Ji J. Sr–Nd–Hf isotopic fingerprinting of transatlantic dust derived from North Africa. *Earth and Planetary Science Letters* 2018, **486:** 23-31.

66. Holz C, Stuut J-BW, Henrich R. Terrigenous sedimentation processes along the continental margin off NW Africa: implications from grain-size analysis of seabed sediments. *Sedimentology* 2004, **51**(5)**:** 1145-1154.

67. Matthewson AP, Shimmield GB, Kroon D, Fallick AE. A 300 kyr high-resolution aridity record of the North African continent. *Paleoceanography* 1995, **10**(3)**:** 677-692.

68. Wilkens RH, Westerhold T, Drury AJ, Lyle M, Gorgas T, Tian J. Revisiting the Ceara Rise, equatorial Atlantic Ocean: isotope stratigraphy of ODP Leg 154 from 0 to 5 Ma. *Clim Past* 2017, **13**(7)**:** 779-793.

69. Manivit H. Calcareous nannofossil biostratigraphy of Leg 108 sediments. In: Ruddiman W, Sarnthein, M., et al., (ed). *Proceedings of the Ocean Drilling Program, Scientific Results, Vol.108*, 1989, pp 35-69.

70. Raffi I, Backman J, Fornaciari E, Pälike H, Rio D, Lourens L*, et al.* A review of calcareous nannofossil astrobiochronology encompassing the past 25 million years. *Quaternary Science Reviews* 2006, **25**(23–24)**:** 3113-3137.

71. Ogg JG. Chapter 5 - Geomagnetic Polarity Time Scale. In: Gradstein FM, Ogg JG, Schmitz MD, Ogg GM (eds). *The Geologic Time Scale*. Elsevier: Boston, 2012, pp 85-113.

72. Wade BS, Pearson PN, Berggren WA, Pälike H. Review and revision of Cenozoic tropical planktonic foraminiferal biostratigraphy and calibration to

the geomagnetic polarity and astronomical time scale. *Earth-Science Reviews* 2011, **104**(1)**:** 111-142.

73. Lisiecki LE, Raymo ME. A Pliocene-Pleistocene stack of 57 globally distributed benthic δ18O records. *Paleoceanography* 2005, **20**(1).

74. Grinsted A, Moore JC, Jevrejeva S. Application of the cross wavelet transform and wavelet coherence to geophysical time series. *Nonlinear processes in geophysics* 2004, **11**(5/6)**:** 561-566.

75. Schulz M, Mudelsee M. REDFIT: estimating red-noise spectra directly from unevenly spaced paleoclimatic time series. *Computers & Geosciences* 2002, **28**(3)**:** 421-426.

76. Weltje GJ, Tjallingii R. Calibration of XRF core scanners for quantitative geochemical logging of sediment cores: Theory and application. *Earth and Planetary Science Letters* 2008, **274**(3–4)**:** 423-438.

77. Weltje GJ, Bloemsma M, Tjallingii R, Heslop D, Röhl U, Croudace IW. Prediction of geochemical composition from XRF core scanner data: a new multivariate approach including automatic selection of calibration samples and quantification of uncertainties. In: Croudace; IW, Rothwell RG (eds). *Micro-XRF Studies of Sediment Cores*. Springer, 2015, pp 507-534.

78. Bloemsma MR. Development of a Modelling Framework for Core Data Integration using XRF Scanning. TU Delft, Delft University of Technology, 2015.

79. Gac J-Y, Kane A. Le fleuve Sénégal: I. Bilan hydrologique et flux continentaux de matières particulaires à l'embouchure. *Sciences Géologiques, bulletins et mémoires* 1986**:** 99-130.

80. Scheuvens D, Schütz L, Kandler K, Ebert M, Weinbruch S. Bulk composition of northern African dust and its source sediments — A compilation. *Earth-Science Reviews* 2013, **116**(0)**:** 170-194.

81. Orange D, Gac J-Y. Bilan géochimique des apports atmosphériques en domaines sahélien et soudano-guinéen d'Afrique de l'Ouest (bassins supérieurs du Sénégal et de la Gambie). *Géodynamique* 1990, **5**(1)**:** 51-65.

82. Orange D, Gac J-Y, Diallo MI. Geochemical assessment of atmospheric deposition including Harmattan dust in continental West Africa. Tracers in Hydrology; 1993: IAHS; 1993.

83. Guieu C, Thomas AJ. Saharan Aerosols: From the Soil to the Ocean. In: Guerzoni S, Chester R (eds). *The Impact of Desert Dust Across the Mediterranean*. Springer Netherlands: Dordrecht, 1996, pp 207-216.

852 84. Criado C, Dorta P. An unusual 'blood rain' over the Canary Islands (Spain).
853 The storm of January 1999. *Journal of Arid Environments* 2003, **55**(4)**:** 765-
854 783.
855
856 85. Viana M, Querol X, Alastuey A, Cuevas E, Rodríguez S. Influence of African
857 dust on the levels of atmospheric particulates in the Canary Islands air quality
858 network. *Atmospheric Environment* 2002, **36**(38)**:** 5861-5875.
859
860 86. Formenti P, Elbert W, Maenhaut W, Haywood J, Andreae MO. Chemical
861 composition of mineral dust aerosol during the Saharan Dust Experiment
862 (SHADE) airborne campaign in the Cape Verde region, September 2000.
863 *Journal of Geophysical Research: Atmospheres* 2003, **108**(D18)**:** 8576.
864
865 87. Linke C, Möhler O, Veres A, Mohácsi Á, Bozóki Z, Szabó G*, et al.* Optical
866 properties and mineralogical composition of different Saharan mineral dust
867 samples: a laboratory study. *Atmospheric Chemistry and Physics* 2006, **6**(11)**:**
868 3315-3323.
869
870 88. Khiri F, Ezaidi A, Kabbachi K. Dust deposits in Souss–Massa basin, South-
871 West of Morocco: granulometrical, mineralogical and geochemical
872 characterisation. *Journal of African Earth Sciences* 2004, **39**(3)**:** 459-464.
873
874 89. Moreno T, Querol X, Castillo S, Alastuey A, Cuevas E, Herrmann L*, et al.*
875 Geochemical variations in aeolian mineral particles from the Sahara–Sahel
876 Dust Corridor. *Chemosphere* 2006, **65**(2)**:** 261-270.
877
878 90. Mounkaila M. Spectral and Mineralogical Properties of Potential Dust Sources
879 on a Transect from the Bodélé Depresseion (Central Sahara) to the Lake Chad
880 in the Sahel. *Hohenheimer Bodenkundliche Hefte* 2006, **78:** 1-311.
881
882 91. Herrmann L, Jahn R, Maurer T. Mineral dust around the Sahara—from source
883 to sink. A review with emphasis on contributions of the German soil science
884 community in the last twenty years. *Journal of Plant Nutrition and Soil*
885 *Science* 2010, **173**(6)**:** 811-821.
886
887 92. Tiedemann R. Acht Millionen Jahre Klimageschichte von Nordwest Afrika
888 und Paläo-Ozeanographie des angrenzenden Atlantiks: Hochauflösende
889 Zeitreihen von ODP-Sites 658-661. Christian-Albrechts-Universität, 1991.
890
891 93. Cohen AS, O'Nions RK, Siegenthaler R, Griffin WL. Chronology of the
892 pressure-temperature history recorded by a granulite terrain. *Contributions to*
893 *Mineralogy and Petrology* 1988, **98**(3)**:** 303-311.
894
895 94. Pin C, Zalduegui JS. Sequential separation of light rare-earth elements,
896 thorium and uranium by miniaturized extraction chromatography: Application
897 to isotopic analyses of silicate rocks. *Analytica Chimica Acta* 1997, **339**(1–2)**:**
898 79-89.
899
900 95. Vance D, Archer C. Isotopic constraints on the origin of Heinrich event
901 precursors. *Goldschmidt Conference Abstract*; 2002.

96. Tanaka T, Togashi S, Kamioka H, Amakawa H, Kagami H, Hamamoto T*, et al.* JNdi-1: a neodymium isotopic reference in consistency with LaJolla neodymium. *Chemical Geology* 2000, **168**(3–4)**:** 279-281.

97. Jacobsen SB, Wasserburg GJ. Sm-Nd isotopic evolution of chondrites. *Earth and Planetary Science Letters* 1980, **50**(1)**:** 139-155.

98. Dietze, E. *et al.* An end-member algorithm for deciphering modern detrital processes from lake sediments of Lake Donggi Cona, NE Tibetan Plateau, China. *Sedimentary Geology* **243-244**, 169-180 (2011).

99. Wood, S. N. *Generalized additive models: an introduction with R*. (CRC press, 2017).

100. Grinsted, A., Moore, J. C. & Jevrejeva, S. Application of the cross wavelet transform and wavelet coherence to geophysical time series. *Nonlinear processes in geophysics* **11**, 561-566 (2004).

101. Hammer, Ø., Harper, D. A. T. & Ryan, P. D. PAST: Paleontological Statistics Software Package for Education and Data Analysis. *Palaeontologia Electronica* **4**, 9 (2001).

102. Castillo, S. *et al.* Trace element variation in size-fractionated African desert dusts. *Journal of Arid Environments* **72**, 1034-1045 (2008).

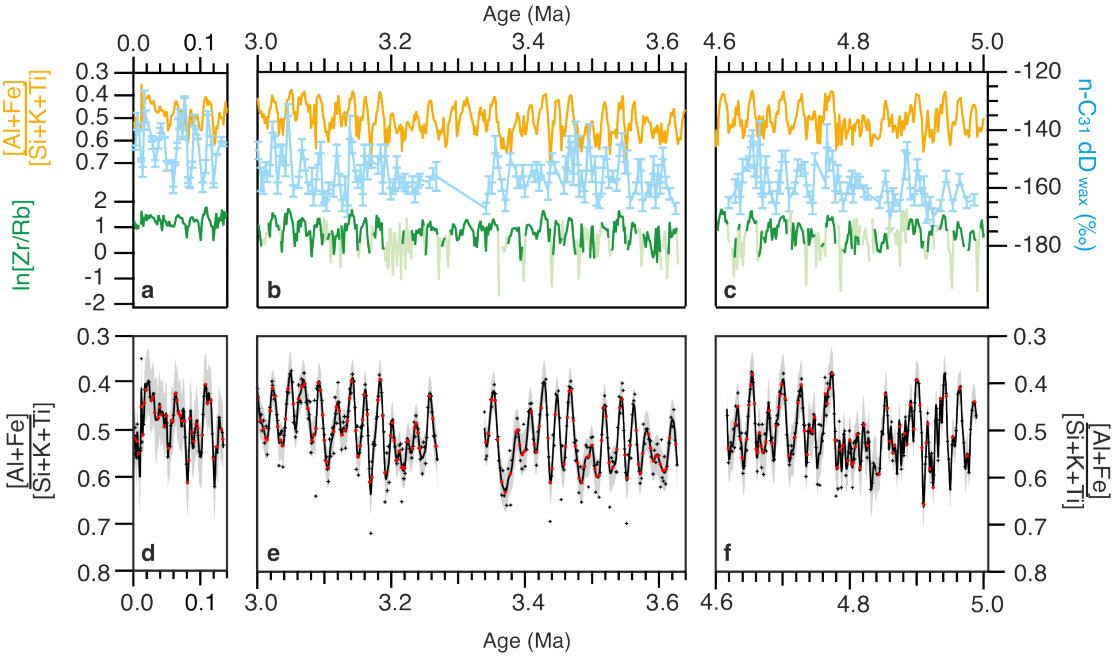

Extended Data Figure 1| Comparison between hydroclimate proxies measured at Site 659. a, b, c Bulk sediment [Al+Fe]/[Si+K+Ti] (orange), δD signatures of C_{31} *n*-alkanes (pale blue, 1σ error bars)[39,40], ln[Zr/Rb] (green, pale colours indicate low element counts). **d, e, f** Generalised additive model (GAM) fit of Site 659 [Al+Fe]/[Si+K+Ti] data shown by black line with grey shaded confidence band (2 standard error). Black crosses indicate original data points with resampled data points used in Kendall's tau-b correlation tests indicated by red circles (see Supplementary Information). **a,d** late Pleistocene, **b,e** late Pliocene, **c,f** early Pliocene.

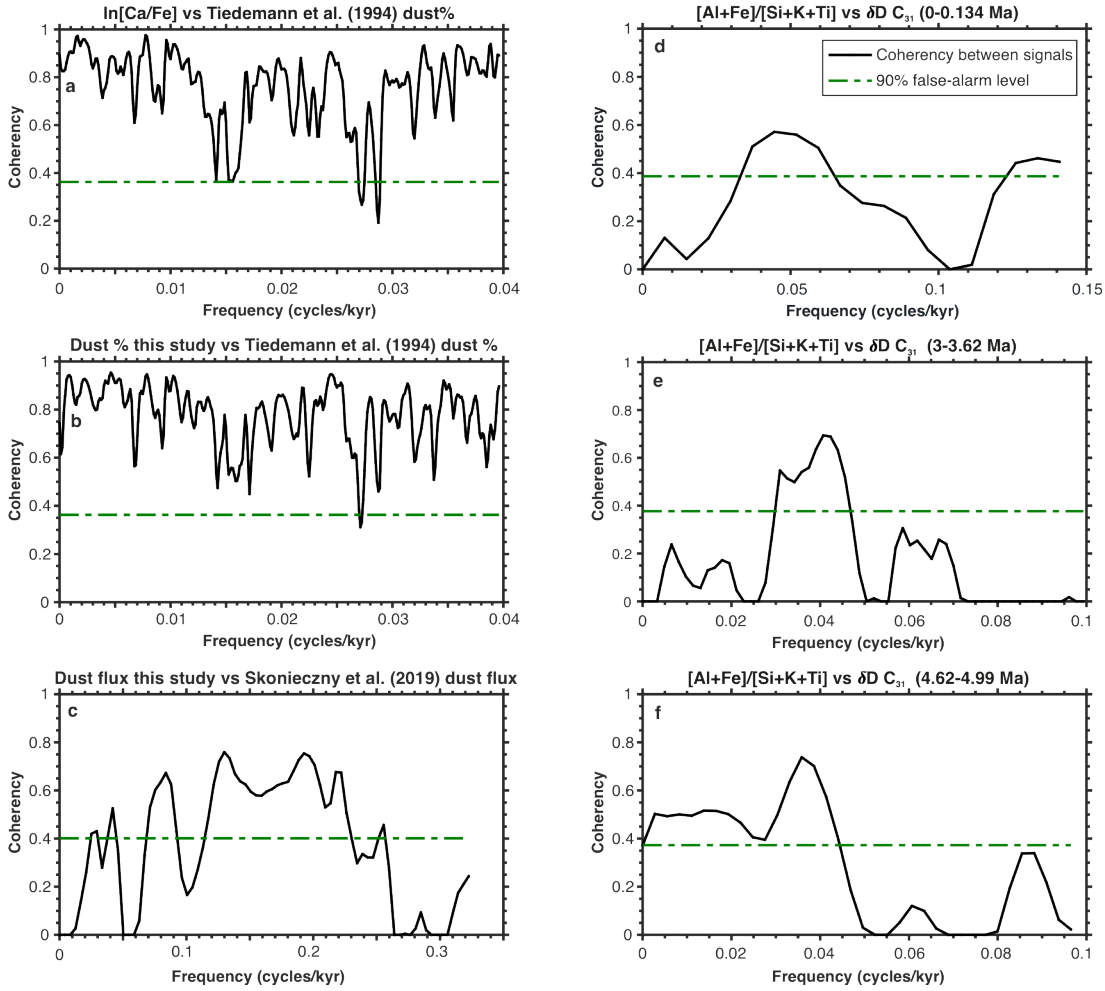

Extended Data Figure 2| Coherency spectra comparing our data from Site 659 to published dust and hydroclimate records from the same and nearby sites. Green dashed line marks 90% Monte Carlo false-alarm level. **a** & **b** Coherency between the dust % estimates from Site 659 of Tiedemann et al. (1994)[2] and our ln[Ca/Fe] (**a**) and dust flux (**b**) estimates over the last 8 Myr. **c** Coherency between our estimated dust fluxes and those of Skonieczny et al. (2019)[15] from nearby site MD03-2705 over the last 240 kyr. **d**, **e**, **f** Coherency between our [Al+Fe]/[Si+K+Ti] values and C_{31} *n*-alkane δD values from Site 659 from Kuechler et al. (2013, 2018)[39,40] for three time slices in the Quaternary (**d**) and Pliocene (**e**, **f**).

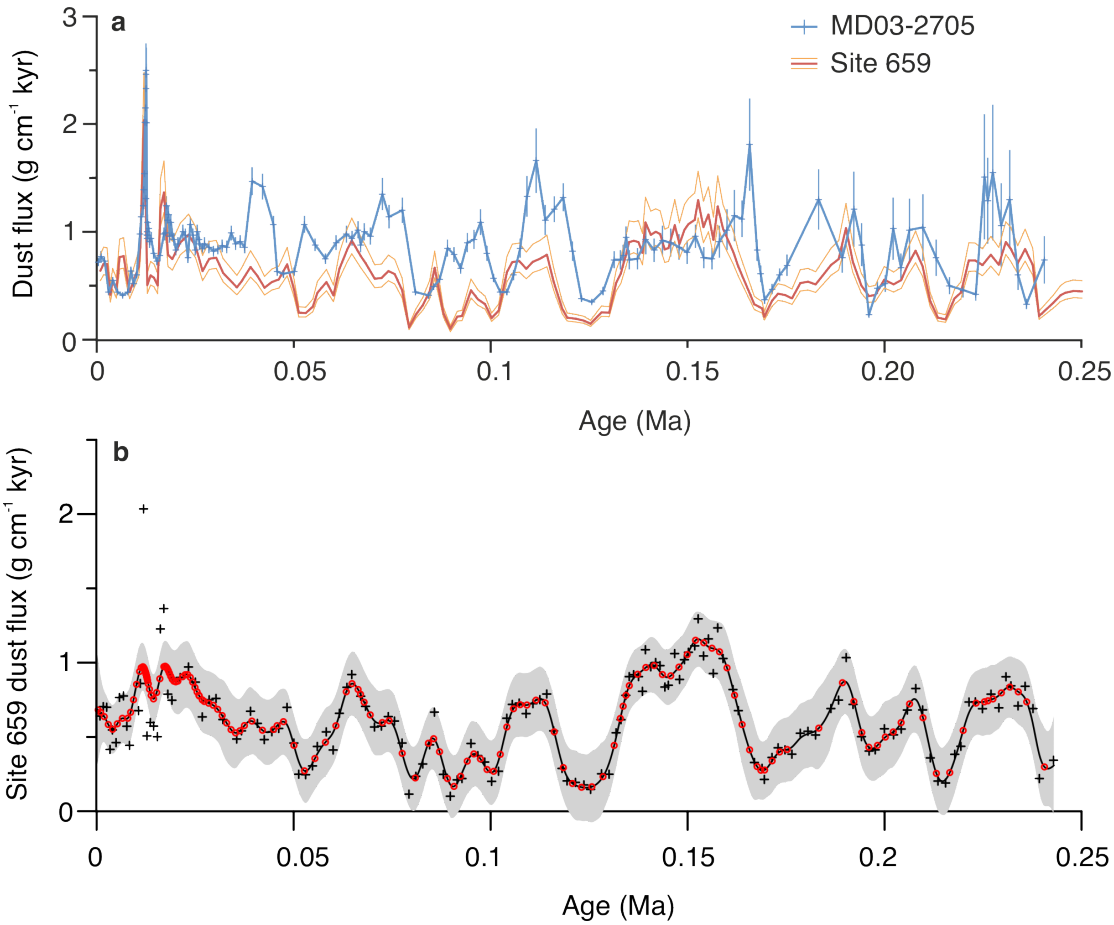

Extended Data Figure 3| Comparison between methods for calculating dust fluxes to marine sediments over the last 250 kyr. a Red: modal dust flux estimates from Site 659 based on a geochemical end-member unmixing approach, with orange lines marking ± 1 standard deviation of 500 realizations. Blue: Dust flux estimates from site MD03-2705 (directly adjacent to Site 659) calculated by ^{230}Th normalization[13] with error bars indicating ± 1 standard deviation. **b** Generalized Additive Model[99] fit of Site 659 median dust fluxes shown by black line with grey shaded confidence band (2 standard error). Black crosses indicate original data points with resampled data points used in Kendall's tau-b correlation tests indicated by red circles (see Supplementary Information).

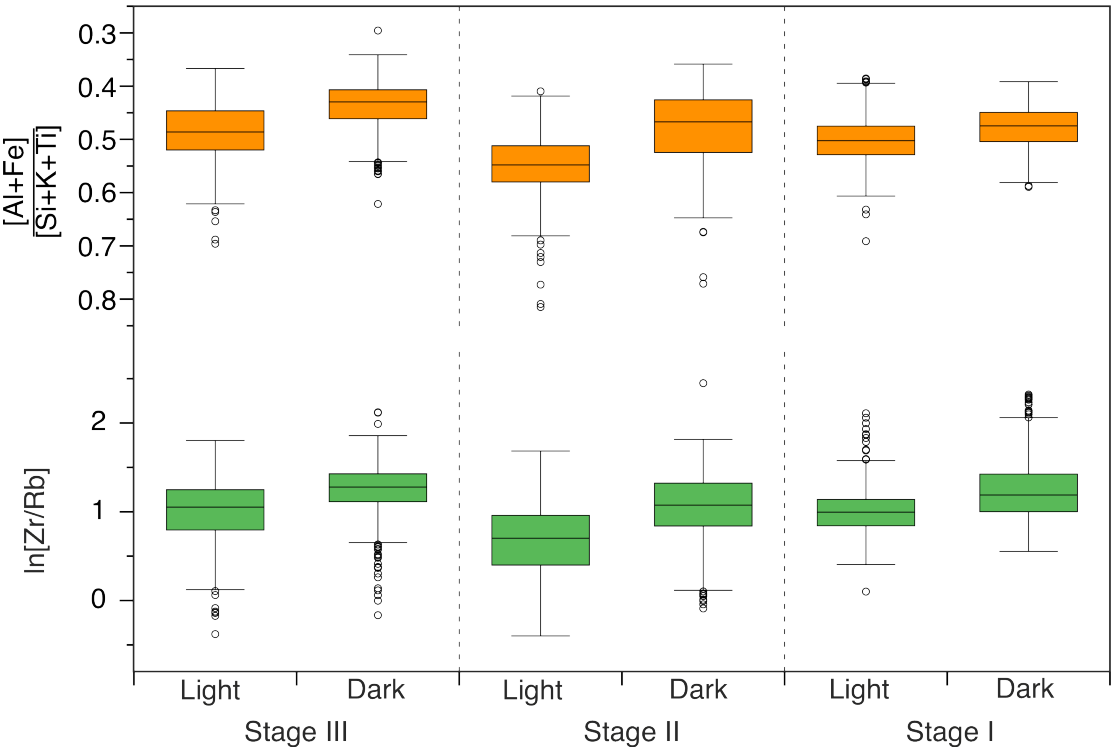

Extended Data Figure 4| Box and whisker plot illustrating co-variation in sediment colour and geochemistry at Site 659. Top: [Al+Fe]/[Si+K+Ti], bottom: ln[Zr/Rb]. Data are plotted from "light" and "dark" sediment layers (as defined by the method described in the Supplementary Information) for each of the three time stages (Stage I: 11.15 – 6.7 Ma, Stage II: 5.75 – 3.5 Ma, Stage III: 2.25 – 0 Ma). Box indicates interquartile range (IQR) with line marking median value, outliers (>1.5 IQR from median) marked with circles and whiskers drawn to the maximum/minimum values excluding outliers. Mann-Whitney-Wilcoxon tests were used to test the null hypothesis that samples from light and dark layers have identical continuous distributions with equal medians for each time interval. All resulting *p*-values were <0.001, giving >99.9% confidence that the differences between light and dark layers are significant.

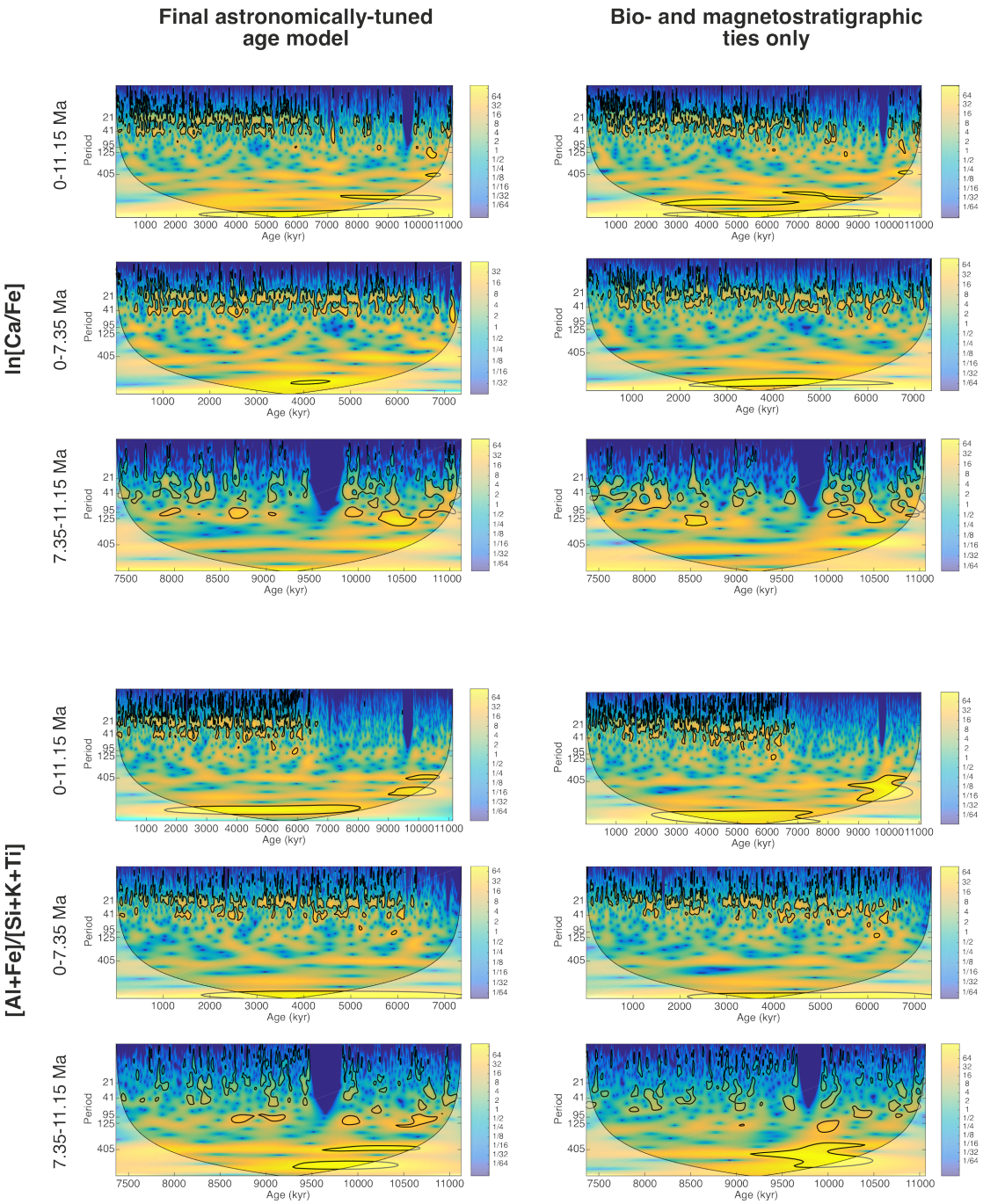

Extended Data Figure 5| Wavelet analysis of Site 659 geochemical records. Comparison between continuous wavelet power spectra of calibrated ln[Ca/Fe] (top) and [Al+Fe]/[Si+K+Ti] (bottom) data on the astronomically-tuned age model (left) and an untuned age model based solely on biostratigraphic and magnetostratigraphic datums[14,69] (right). Thick black contours designate the 5% significance level against red noise and the cone of influence is shown as a lighter shade, where edge effects may cause distortion. Data were detrended and smoothed (5-pt moving average) prior to the wavelet analyses. Separate spectra were also generated for the older and younger sections of the full record to reduce the impact of temporal changes in cycle amplitude on the detected frequencies. Analyses were performed and figures generated using the Matlab code of Grinsted et al. (2004)[100]. See Supplementary Information for further discussion.

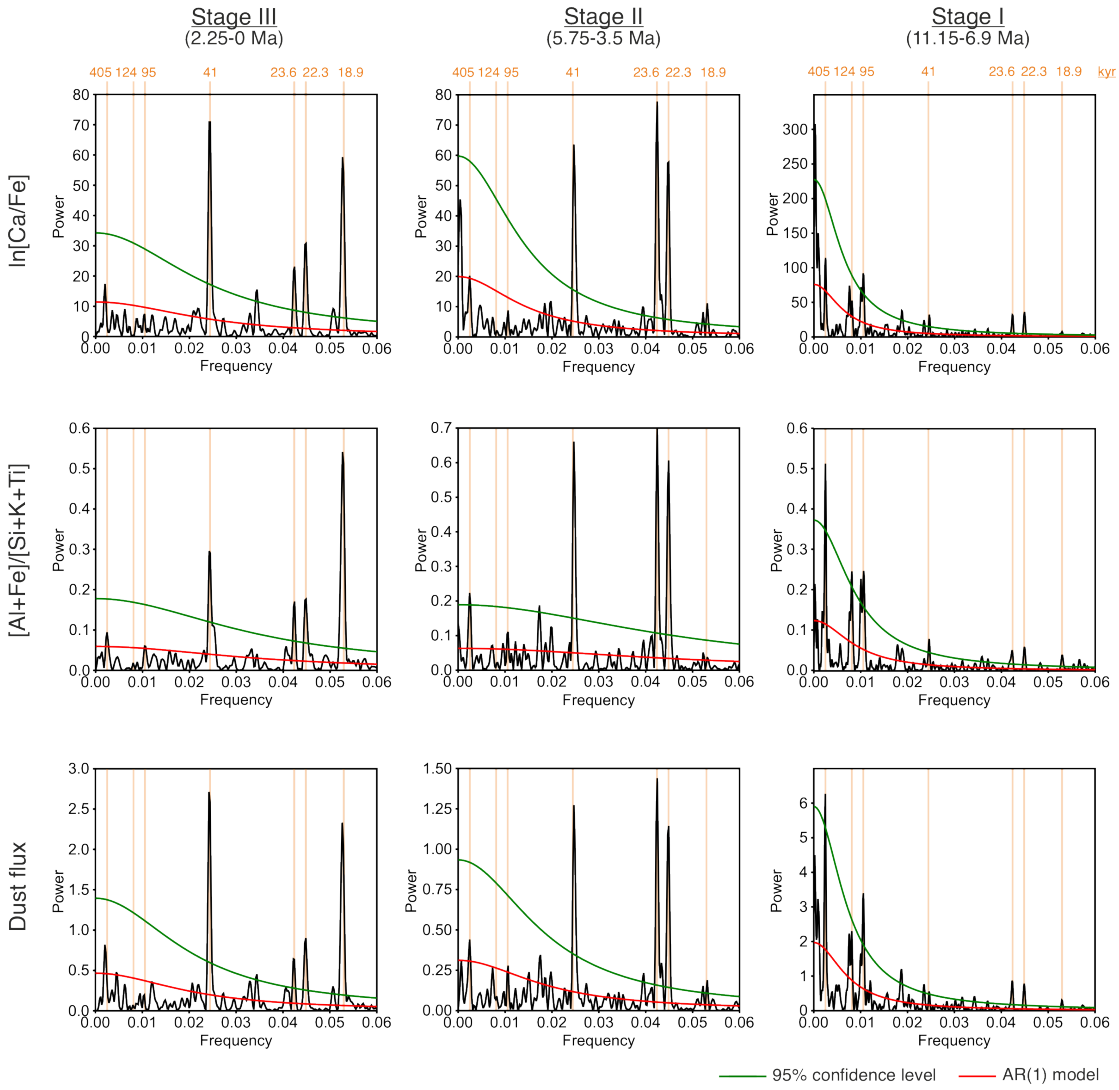

Extended Data Figure 6| REDFIT spectral analysis[75] of Site 659 geochemical records. Top: ln[Ca/Fe] ratios, middle: calibrated [Al+Fe]/[Si+K+Ti] ratios, bottom: median dust flux values. Data are divided into the three time stages discussed in the text. Left: Stage III (2.25–0 Ma), centre: Stage II (5.75–3.5 Ma), right: Stage I (11.15–6.9 Ma). Green curves mark the false-alarm level at the 95% confidence level, red curves indicate AR(1) red noise models. Orange lines and numbers indicate the frequencies equivalent to periods (in kyr) of major astronomical cycles (precession, obliquity and eccentricity). Analysis performed and figures created using PAST software[101]. See Supplementary Information for further discussion.

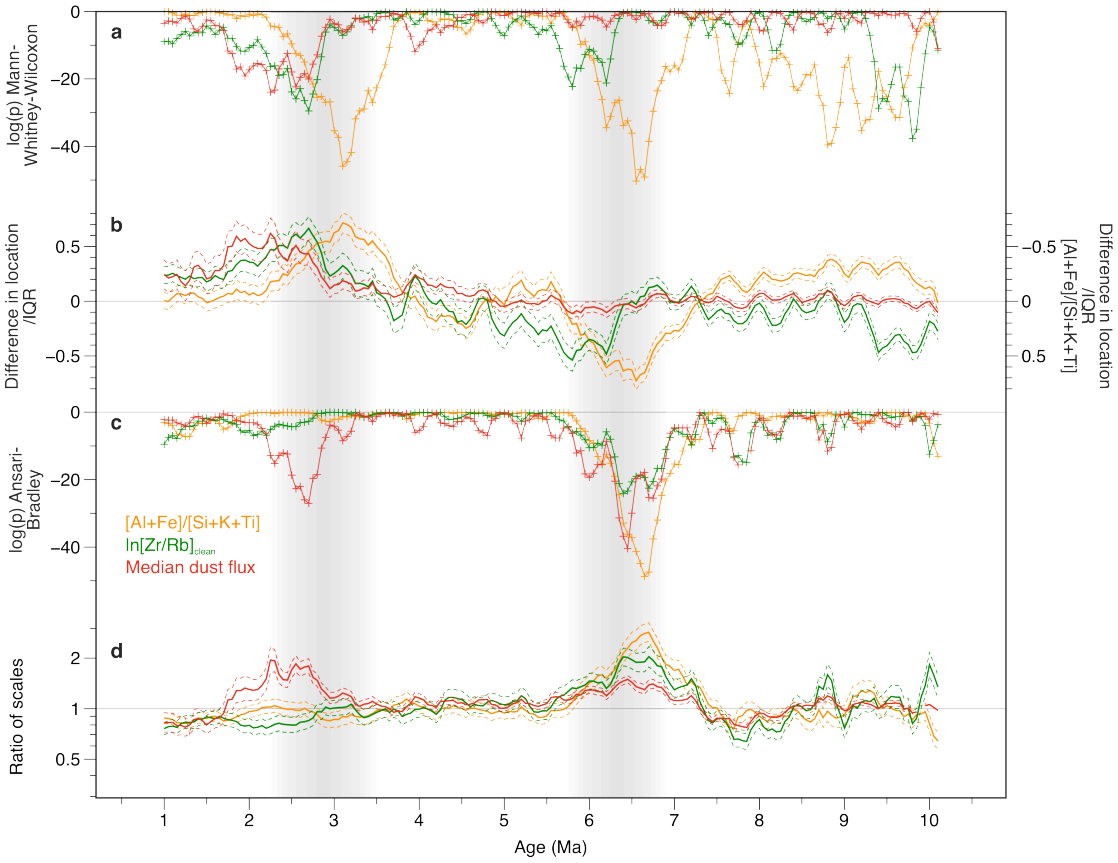

Extended Data Figure 7| Running statistical analysis of Site 659 geochemical data, comparing 1 Myr data bins. a Mann-Whitney-Wilcoxon test log(p) values to detect shifts in central tendency (see Supplementary Information). Low values indicate extremely low probabilities that the two data bins have the same central tendency. **b** Estimated difference in location between the two data bins divided by the interquartile range of the complete data set, with 95% confidence interval plotted. Note that [Al+Fe] is plotted on an inverted axis. **c** Ansari-Bradley test log(p) values to detect shifts in dispersion. Low values indicate extremely low probabilities that the two data bins have the same dispersion. **d** Ratio of scales between the two data bins, with 95% confidence interval plotted. Orange: calibrated [Al+Fe]/[Si+K+Ti], green: ln[Zr/Rb] (with XRF counts <300 removed), red: median dust flux (g cm^{-2} kyr^{-1}). Grey shading indicates intervals of greatest change in the geochemical time series revealed by statistical analyses.

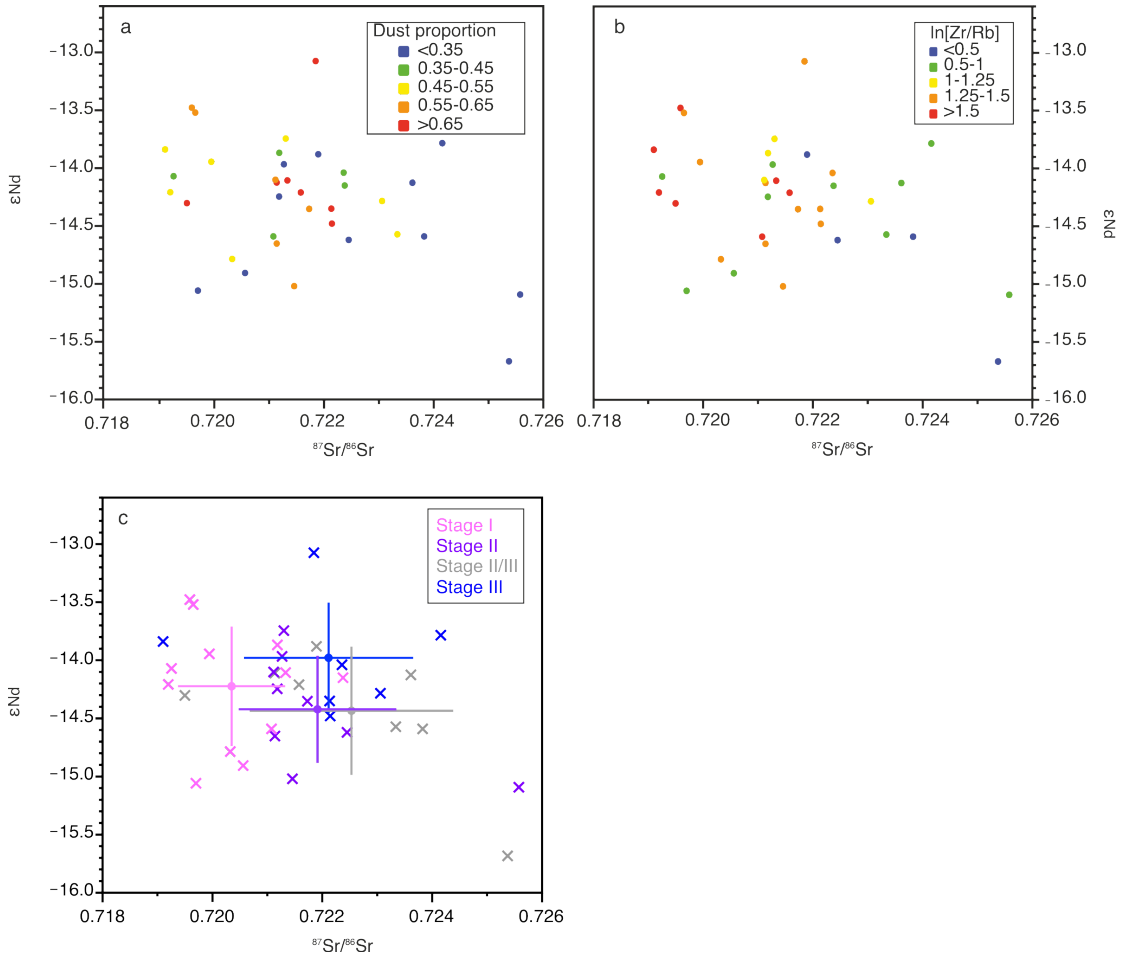

Extended Data Figure 8| Cross-plots of strontium and neodymium isotopic signature of lithic fraction of Site 659 sediments. Data coloured by: **a** the proportion of the lithic fraction attributed to dust by end-member unmixing ([dust]/[dust+riverine]), **b** co-registered ln[Zr/Rb] values. Red marks samples dominated by dust/coarse grains, blue marks samples dominated by riverine inputs/fine grains. **c** Data coloured by age, where stage I (pink) is the oldest (>6.9 Ma) and stage III (blue) is the youngest (<2.25 Ma) and grey indicates samples from the transition between stages II and III (3.5–2.25 Ma). Individual samples are marked by crosses and mean values for each age range shown by circles, with error bars indicating 1 standard deviation.

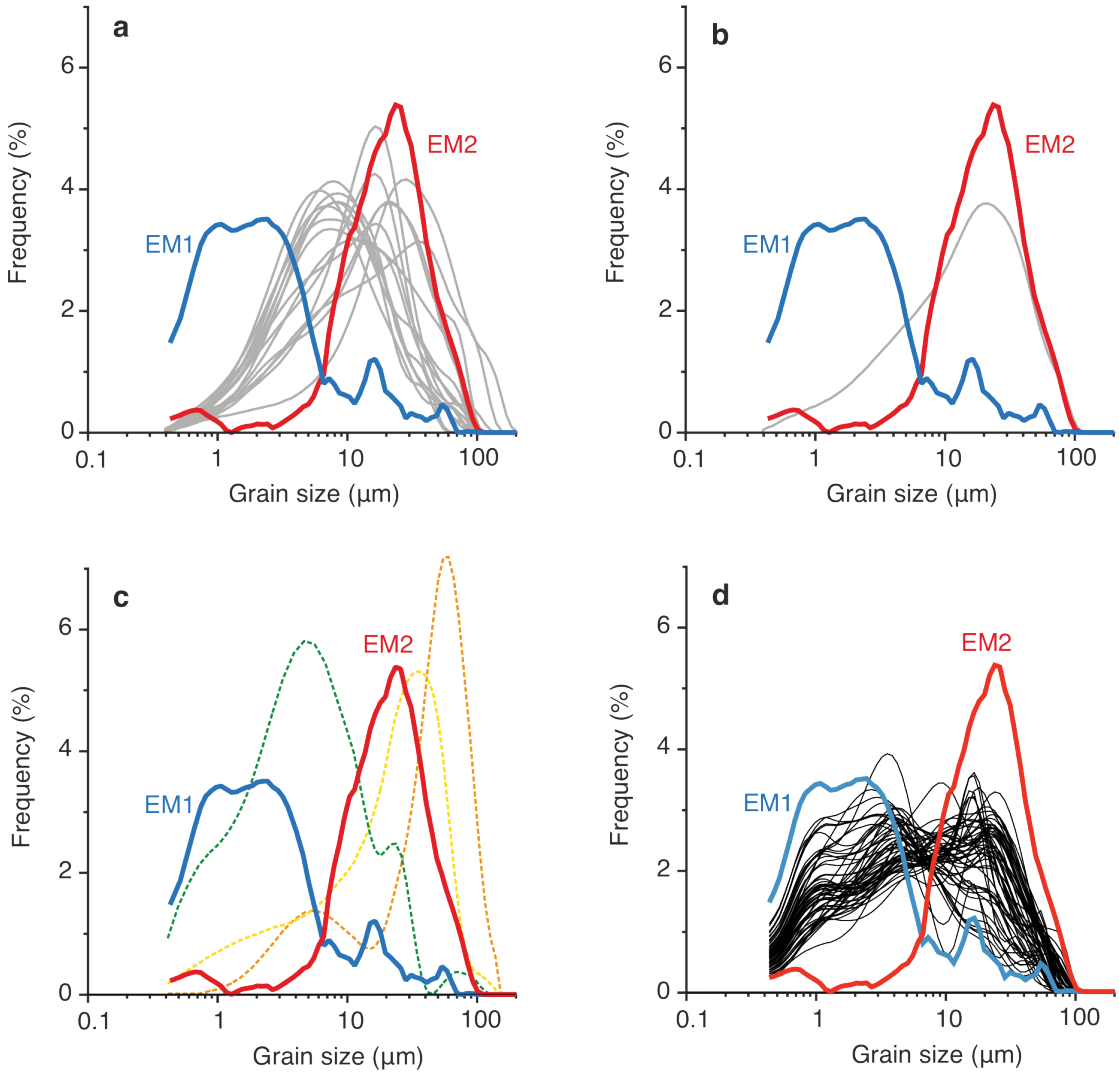

Extended Data Figure 9| Grain size distributions of the end-members calculated from the lithic fraction of ODP Site 659. Grain size derived end-member 1 (EM1) in blue and grain size derived end-member 2 (EM2) in red compared to: **a** Modern dust samples recorded offshore NW Africa from Stuut et al. (2005) in grey[64]. **b** As (a) but with just the most proximal measurements to Site 659 (M41/1 D4, centered at 19.73°N, 17.91°W) plotted. **c** The grain size end members of Tjallingii et al. (2008) from site GeoB7920-2 (20.75°N, 18.58°W)[12]. Yellow and orange dashed lines indicate the end members attributed to fine and coarse dust respectively, with the riverine end member shown in green. **d** All Site 659 lithogenic grain size distributions (black).

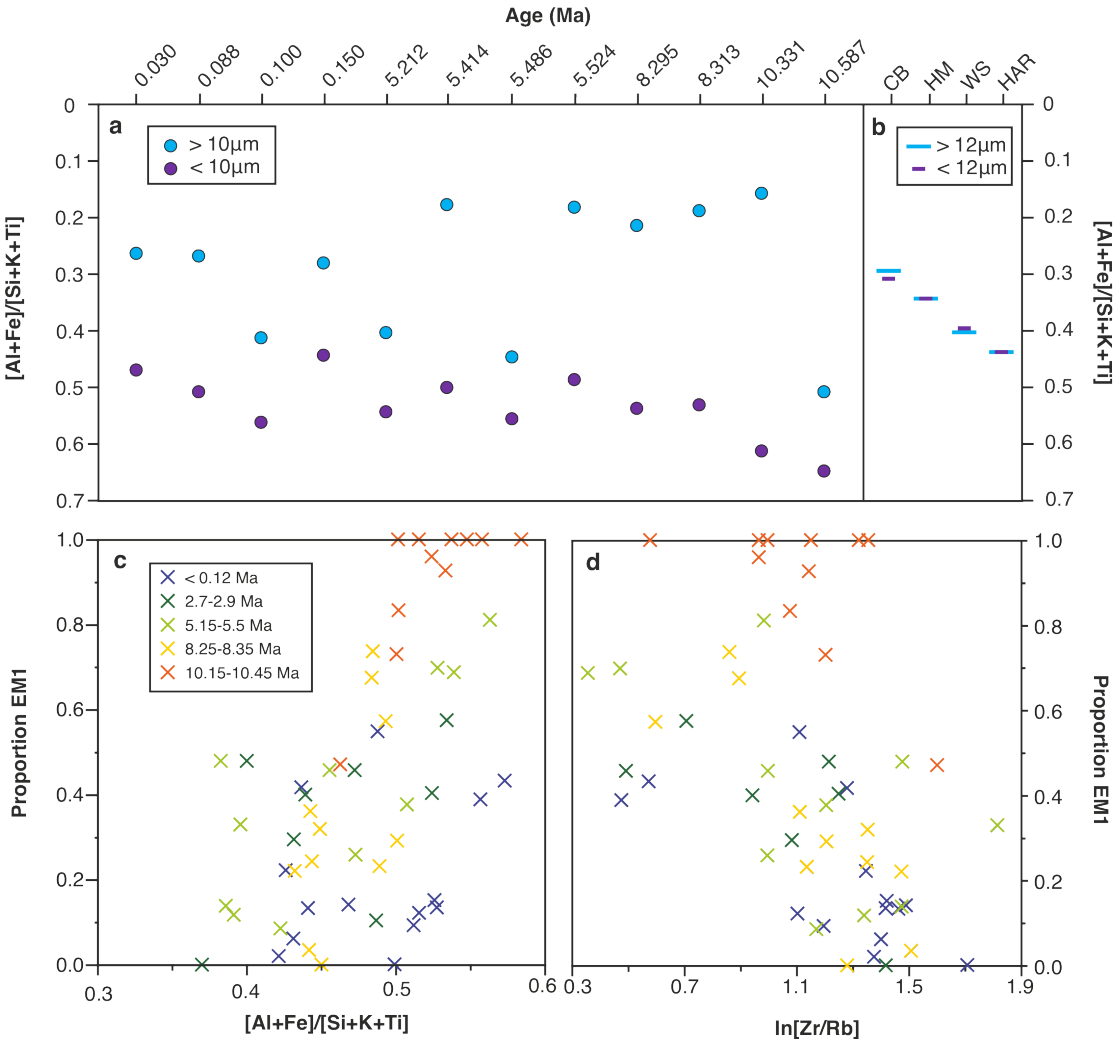

Extended Data Figure 10| Comparisons between grain size and geochemical proxies at Site 659. **a & b** [Al+Fe]/[Si+K+Ti] ratios of the coarse and fine fractions of **(a)** 12 sediment samples from Site 659 sieved at 10µm and analysed by discrete XRF analysis with sample ages are listed along the top and **(b)** desert surface soil and aeolian dusts from four locations in the Sahara-Sahel dust corridor, analysed by inductively coupled plasma mass spectrometry and grouped into <12 µm and >12 µm size fractions, from Castillo et al. (2008)[102]. CB: Chad Basin, HM: Hoggar Massif, WS: Western Sahara, HAR: Harmattan. **c** and **d** The proportion of lithogenic grain size derived end-member 1 (grain size EM1, attributed to fine riverine inputs) plotted against the sediment geochemical ratios **c** [Al+Fe]/[Si+K+Ti] and **d** ln[Zr/Rb]. Data points are coloured by sample age, where the youngest samples are in blue and the oldest in orange.

Supplementary Information

For: Astronomically controlled aridity in the Sahara since at least 11 million years ago

Anya J. Crocker, B. David A. Naafs, Thomas Westerhold, Rachael H. James, Matthew J. Cooper, Ursula Röhl, Richard D. Pancost, Chuang Xuan, Colin P. Osborne, David J. Beerling, Paul A. Wilson

Supplementary Discussion

Comparison to published dust reconstructions

Reconstructions of the flux of dust from the African continent deposited in ODP Site 659 sediments over the past 5 Myr were originally published by Tiedemann et al. (1989)[1] and Tiedemann et al. (1994)[2]. Their records are based upon the assumption that the proportion of dust in the sediment can be approximated from the non-carbonate fraction (=100–%$CaCO_3$). We find an excellent correlation between the discrete measurements of these earlier studies (which include a range of analytical techniques)[1] and ln[Ca/Fe] values measured by XRF core scanning (Supplementary Figure 4). A Kendall's tau-b correlation test between the dust % estimates of Tiedemann et al. (1994)[2] and those presented here reveals a positive, extremely significant correlation ($\tau = 0.669$, *p*-value <0.001), with a comparison between published dust % to ln[Ca/Fe] revealing an even stronger (but negative) correlation ($\tau = -0.711$, p-value <0.001). These results show that our ln[Ca/Fe] data provide reliable down core records of terrigenous sediment content at ODP Site 659. We note, that these datasets, in common with many palaeoclimate records, likely show autocorrelation (where there is a degree of similarity between a time series and a lagged version of itself). This acts to elevate the calculated correlation coefficients between data series. We therefore also show coherency spectra, calculated using the REDFIT-X program of Ólafsdóttir et al. (2016)[3]. This approach uses a Lomb-Scargle Fourier transform to perform cross-spectral analyses between unevenly spaced data sets. Monte Carlo simulations that mimic key properties of the datasets (e.g. autocorrelation and time spacing) are used to estimate the false-alarm level for the calculated coherency. These spectra are shown in Extended Data Figure 2. Significant coherency between the dust % estimates of Tiedemann et al. (1994) and both our ln[Ca/Fe] and dust % estimates across almost all frequencies supports the strong agreement among the different techniques (Extended Data Figure 2a,b).

Recent work has shown that, in addition to dust inputs, fine-grained riverine sediment is a likely contributor to Site 659 and the nearby continental margin[4,5]. We therefore partitioned the bulk terrigenous sediment component into two separate components (classified as riverine and aeolian) by applying an unmixing approach (Methods). Our absolute dust fluxes are therefore lower than those of Tiedemann et al. (1994)[2] (Supplementary Figure 4), which were calculated by assuming that all terrigenous material at Site 659 was wind-blown in origin. Nevertheless, for the last 5 Myrs, where there are detailed records from Tiedemann et al. (1994)[2], the down core trends in the data yielded by the two different approaches are generally very consistent over both secular and astronomical timescales.

For sediments younger than about 200 to 300 kyr, thorium-normalization of sediment accumulation rates has been used to provide age control independent of sediment focusing and dissolution along the NW African margin[6-10]. To assess whether these processes likely exerted a major control over our dust flux reconstructions we compared our calculated fluxes to those from site MD03-2705[9] (18°05′N, 21°09′W). Because dust flux estimates were calculated at

different age points between the two sites, we calculated generalized additive models (GAMs)[11] using R[12] to create a smoothed fit to our datasets and resampled this at ages corresponding to the ^{230}Th-normalised data points (Extended Data Figure 3). This approach provides a good representation of the original dataset, except for the most recent 20 kyr, where GAMs struggle to capture the high frequency, high magnitude variability seen at both Site 659 and MD03-2705. The degree of correlation between the two dust flux reconstructions was then assessed using a Kendall's tau-b correlation test. Despite uncertainty introduced by the GAM approximations and chronological uncertainties between the two sites, we find a positive, strongly significant correlation ($\tau = 0.298$, p-value <0.001) between our dust fluxes at Site 659 and those calculated by ^{230}Th-normalisation at proximal site MD03-2705[9] (Extended Data Figure 3). We also performed cross-spectral analysis between the two datasets using REDFIT-X[3] (where no resampling is required). The results of these analyses indicate that there is largely significant coherency between data sets across the frequency range 0.025–0.23 cycles/kyr (Extended Data Figure 2c), equivalent to periodicities of 40–4 kyr. These results suggest that our dust flux reconstructions are representative of aeolian transport from the continent and not major sediment redistribution in the ocean or rapid pulses of dissolution, at least over the past 240 kyr where ^{230}Th-normalised dust flux estimates exist.

Comparison to established XRF ratios and other hydroclimate proxies

Our discussion focuses on two geochemical ratios ([Al+Fe]/[Si+K+Ti] and ln[Zr/Rb]) provided by our XRF work but our interpretations gain further support from three other elemental ratios that have also been shown to closely track climatic gradients along the African coastline today. Ti/Al is proposed as a proxy for aeolian versus fluvial input and Fe/K and Al/Si are suggested as tracers of terrestrial climatic zones[13], although Al/Si can also be influenced by high siliceous microfossil concentrations at times of intense upwelling[14]. All three of these ratios agree very closely with one another and with [Al+Fe]/[Si+K+Ti] over astronomical timescales throughout our records (Supplementary Figures 5 and 6). Dark sediment layers consistently record high ln[Ti/Al] values and low ln[Fe/K] and ln[Al/Si] values, indicating a dominance of aeolian over riverine sediment and a decrease in the intensity of chemical weathering, a trend documented with increasing aridity associated with increasing distance from the equator today[13]. These findings strongly support our interpretation that the dark sediment bands represent dust pulses associated with increased aridity throughout the last 11 Myr.

The different elemental ratios also show clear similarity over multi-million year timescales. The onset of more extreme wet events between 7 and 6 Myr can be seen in all ratios, as can a shift towards more arid conditions over the past ~3 Myr. A decrease in ln[Al/Si] through the Pliocene and Pleistocene is more pronounced than the other ratios, and, given the very low concentrations of siliceous microfossils recorded in the Site 659 sediments[15], may indicate an increase in the proportion of silica-rich terrigenous material reaching the site, such as pale quartz grains from coastal sources[16].

We also compare our [Al+Fe]/[Si+K+Ti] and ln[Zr/Rb] data to an independent hydroclimate proxy: the hydrogen isotopic (δD) signature of *n*-alkanes (Extended Data Figure 1). These compounds are found as leaf waxes in terrestrial plants, with δD values at Site 659 suggested to largely depend upon the amount of rainfall, although differences in plant physiology (e.g. photosynthetic pathway, rooting depth and leaf anatomy) and climate (e.g. moisture source region, evaporation) can also influence plant wax δD signatures[17]. Extended Data Figure 1 illustrates the strong agreement between C_{31} *n*-alkane δD values and our XRF-based hydroclimate proxies during several snapshots of the Pliocene and Pleistocene (where δD data are available)[18,19].

We also test the similarity between the datasets statistically. Our data and the reported δD values are from the same site but different sample sets were used so we apply GAMs to create a smoothed fit to our [Al+Fe]/[Si+K+Ti] record and resample it at the matching depths to the δD data (Extended Data Figure 1d-f). Separate fits were made for 0.14–0 Ma, 3.27–3 Ma, 3.63–3.34 Ma, 4.83–4.61 Ma and 4.99–4.83 Ma to ensure that the GAMs captured astronomical-scale variability. We combined the data from all of the time windows to perform a Kendall's tau-b correlation test with the full δD dataset, which revealed a negative, strongly significant correlation with [Al+Fe]/[Si+K+Ti] (τ = -0.218, *p*-value <0.001). Note that a negative correlation indicates agreement between the proxies, with higher [Al+Fe]/[Si+K+Ti] values but more negative δD values indicating a wetter climate. The strength of the relationship between our XRF data and the δD results (Extended Data Figure 1a-c) support the use of [Al+Fe]/[Si+K+Ti] to reconstruct past changes in continental hydroclimate in these sediments.

We also performed cross-spectral analysis to assess how the coherency of [Al+Fe]/[Si+K+Ti] and δD varies with frequency (Extended Data Figure 2d-f). These analyses were carried out for three separate time slices due to the discontinuous nature of available high-resolution δD data. We find the strongest coherency occurs at frequencies of ~0.03–0.05 cycles/kyr, implying that these records are coherent over precessional timescales, both responding to insolation-forced variability in hydroclimate. Outside this range, the coherency is lower. This result may indicate the influence of secondary processes acting on one or both proxies over different timescales.

Geochemical differences between light and dark layers

Colour data were generated from the central portion of ODP core photograph images[15] along our splice using Code for Ocean Drilling Database macros[20], with an average sample spacing of ~2mm. Lightness values of >80 or more than 3 standard deviations above or below a 4 cm rolling mean value were excluded to filter out artefacts such as cracks and core gaps from the dataset. Lightness data were then smoothed by calculating the mean value over a 4 cm rolling window.

To identify "light" and "dark" sediment layers, we filtered out longer-term variability in the lightness data by calculating residuals from a 5 m rolling mean. The residual dataset was then resampled to match the depths corresponding to XRF data using simple linear interpolation. "Light" layers were defined as those with residual lightness values greater than the 60% percentile of the rolling 5 m window, while dark layers were defined as those with lightness values below the 40% percentile.

Extended Data Figure 4 illustrates the geochemical differences between sedimentary layers classified as "light" and "dark" in the Site 659 XRF datasets. Mann-Whitney-Wilcoxon tests were used to identify whether there were significant geochemical differences between the light and dark layers for each of our three time intervals. Extremely low *p*-values (<0.001) are documented for both [Al+Fe]/[Si+K+Ti] and ln[Zr/Rb] in each of the three time windows, which shows that there are clear, highly significant geochemical differences between light and dark sediment layers at Site 659.

Identification of change points in time series

To identify the intervals of greatest change in our geochemical time series, we applied running Mann-Whitney-Wilcoxon (also known as Wilcoxon rank sum) and Ansari-Bradley statistical tests, following the approach of Trauth et al. (2009)[21]. We test whether samples taken from 1 Myr ranges either side of a selected age come from distributions with the same properties, or

whether there were significant differences between them. We used 1 Myr bins to smooth out the influence of shorter frequency astronomical variability and highlight secular changes in the datasets.

[Al+Fe]/[Si+K+Ti], ln[Zr/Rb] and median dust flux data sets were each resampled using simple linear interpolation to give an average data resolution of 2 kyr. A Mann-Whitney-Wilcoxon test was applied to test the null hypothesis that samples from the million years preceding and postdating the chosen date were selected from identical continuous distributions with equal medians.

The Ansari-Bradley test determines whether two samples come from continuous distributions with the same median and shape but different dispersions. As the results of the Mann-Whitney-Wilcoxon test indicate that there are significant shifts in the median values of all three of our proxy data sets between different time windows, we calculate the difference of each data point from the whole-core mean and then adjust these residuals by the difference in location between the two time windows (the median of the difference between a sample from each of the two distributions). Due to the size of the datasets, a normal approximation was used when calculating the *p*-values.

The results of the running Mann-Whitney-Wilcoxon and Ansari-Bradley tests on our three proxy datasets reveal two major intervals of change in our time series; 6.9–5.75 Ma and 3.5–2.25 Ma (Extended Data Figure 7). The first interval is marked by a major increase in the variability of all three proxy records from 6.9–6.3 Ma, accompanied by an increase in the central tendency of [Al+Fe]/[Si+K+Ti] values. This is followed by a decrease in ln[Zr/Rb] values (6.2–5.75 Ma).

During the second key interval of change, a decrease in the central tendency of [Al+Fe]/[Si+K+Ti] (centred around 3.2–3.1 Ma) again leads change in the ln[Zr/Rb] data (which shows an increase centred around 2.8–2.25 Ma), although this time there is also an increase in the mean dust flux values approximately synchronous with the change in ln[Zr/Rb]. There is a shift to greater dispersion in the dust fluxes centred around 2.7 Ma, but no concurrent change in the amplitude of variability of [Al+Fe]/[Si+K+Ti] or ln[Zr/Rb].

Attribution of sedimentological end-members

Our two lithogenic grain size end-members identified at Site 659 have clearly distinct grain size distributions. End-member EM1 is by far the finer of the two, with modal grain sizes of 0.7–4 μm. End-member EM2 has a sharp, unimodal distribution dominated by grains of 10–40 μm diameter.

There is remarkable agreement between the grain size distributions of Site 659 lithogenic end-member 2 (EM2) and dust samples taken offshore NW Africa[22], particularly those sampled closest to Site 659 (Extended Data Figure 9). EM2 is also similar to the fine dust end-member identified at NW African site GeoB7920-2 by Tjallingii et al. (2008)[4] (Extended Data Figure 9). We therefore attribute EM2 to windblown dust exported from the African continent.

The origin of EM1 is less immediately obvious. Distal dusts transported long distances from their sources are suggested to have volume median grain sizes of ca. 2–7 μm[23-26], therefore, it is possible that EM1 at Site 659 also represents a dust component, albeit much finer than EM2. However, Site 659 end-member 1 (EM1) contains a much higher proportion of grains <2 μm than any of the atmospheric dust samples recorded offshore northwestern Africa by Stuut et al. (2005)[22] (Extended Data Figure 9a), and is finer than either samples dominated by either wet or dry deposition captured by sediment traps offshore Cape Blanc[27]. EM1 is also finer than

modern African dust captured across the Atlantic throughout the year and more distal African-sourced dust in Puerto Rico[23,28,29]. These observations strongly suggest that EM1 is unlikely to represent a pure dust component, at least under wind conditions similar to modern.

We note that EM1 has a very strong similarity to the grain size distribution of the fine lithogenic end-members identified by both Holz et al. (2004)[30] and Tjallingii et al (2008)[4], which are attributed to distal rain-out of fine particulates from riverine sources. Networks of river channels, active during past intervals of humidity have been identified across North Africa, many of which drain into the Atlantic[5,31], with submarine channels transporting this material into the deep ocean[32,33]. A distal riverine interpretation for fine-grained sediments at Site 659 is supported by high proportions of the fine end-member in core top sediments offshore Morocco which receive sediment from the Souss River[30] and the fact that highest proportions of this fine end-member occur at times where enhanced rainfall is well evidenced in North Africa, such as African Humid Period 1[4,34], although increased fluxes of fine sediments are not consistently observed at all sites on the northwest African margin at this time[8]. The elevated location of Site 659 on the Cape Verde Plateau means that hypopycnal transport would likely be required for material of riverine origin to reach the site. EM1 at Site 659 is slightly finer than the riverine end-member identified at site GeoB7920-2[4] (Extended Data Figure 9c), which is consistent with the greater distance from the continent of Site 659 compared to GeoB7920-2 and the requirement for sediment to be suspended within the water column to reach Site 659 due to its elevated position on the Cape Verde Rise (Supplementary Figure 1).

A third possible contributor to EM1 is resuspension of sediments from the continental shelf. Although shelf sediments are dominated by grains much coarser than the aeolian inputs, potentially representing relict dune fields[35], fine grained components are preferentially transported in nepheloid layers[36]. Nepheloid layer activity is currently very low around Cape Verde[37,38], however, a contribution of these processes to Site 659 cannot be ruled out.

To further explore the origin of EM1, we test for geochemical differences between the fine and coarse components of the sediments. 12 samples with a range of ages and lithologies were wet sieved at 10 μm (close to the boundary between EM1 and EM2 dominance) to separate out the coarse and finer fractions. Samples were then oven dried and homogenized, then mixed with di-lithium tetraborate and fused to create beads. These were analysed by X-ray fluorescence using a Phillip MagiX Pro WD-XRF at the University of Southampton Waterfront Campus, NOCS, calibrated using international rock standards prepared in the same way as our samples.

All 12 of our samples show a clear offset in [Al+Fe]/[Si+K+Ti] between the >10 μm and <10 μm size fractions (Extended Data Figure 10a). The <10 μm [Al+Fe]/[Si+K+Ti] values are 0.11–0.46 greater than the <10 μm fraction, which means that the fine grained components plot much closer to the value of suspended sediments from the Senegal River than the coarse fractions do. The largest size fraction differences are generally recorded in the Miocene aged samples from depths with high terrigenous contents (indicated by high ln[Fe/Ca] values and a dark colour). In addition, there is a strong correlation between the relative proportions of grain-size end-members and our geochemical ratios for past dust inputs (Extended Data Figure 10c,d). High proportions of EM1 are associated with both high [Al+Fe]/[Si+K+Ti] values (similar to modern riverine inputs) and low ln[Zr/Rb] values which are commonly interpreted as indicating a dominance of fine-grained clays over coarse dust[4,39]. These results are strongly supportive of a distal riverine contribution to EM1.

We note that differences in major element compositions might also be expected between coarse and fine fractions of a purely aeolian sample due to the susceptibility of different minerals with different chemical compositions to be weathered into finer particles. However, samples of dusts and dust source sediments from across the Sahara-Sahel dust corridor show negligible offsets in [Al+Fe]/[Si+K+Ti] between size fractions (Extended Data Figure 10b)[40]. Therefore, we suggest that the differences we record in major element signatures between the <10 μm and >10 μm size fractions reflect inputs from multiple sources rather than size-dependent fractionation from a single source.

The higher [Al+Fe]/[Si+K+Ti] values of the <10 μm sediment component (Extended Data Figure 10) mean that our geochemical unmixing approach acts to remove this very fine component. Therefore, even if EM1 is dominantly derived from resuspended shelf material rather than distal riverine material, the geochemical unmixing approach will still act to remove its contribution from the total lithogenic component to produce our dust flux estimates. If EM1 contains a component of fine-grained dust, then our dust flux estimates are likely to be underestimates.

In conclusion, a dominantly distal riverine origin for EM1 is indicated by: (i) grain size distribution analyses showing that EM1 is very similar to the fine end-member previously identified at higher concentrations during humid time intervals[4,34] and at latitudes to the north of the Sahara where precipitation is higher[30] (ii) EM1 is much finer than either proximal or distal North African dust (including samples from as far as the Caribbean)[22,23,29,41], (iii) large geochemical differences between the coarse and fine fractions of Site 659 sediments are too great to be explained by size-dependent fractionation from a single source, and (iv) the current absence of major nepheloid layer activity around Cape Verde[37,38].

Effects of grain size on radiogenic isotope signatures

A grain size effect on Sr isotope signatures of sedimentary lithics has previously been documented including in African dust, with fine-grained samples having higher $^{87}Sr/^{86}Sr$ values, although a similar effect in Nd isotopes is not commonly observed[42-44]. We find no strong relationship between the radiogenic isotopic signature and either the proportion of dust or the grain size of the sediment as approximated by ln[Zr/Rb] (Extended Data Figure 8a,b), although we note a tendency for samples with the most radiogenic Sr and unradiogenic Nd isotope signatures to have low ln[Zr/Rb] values and be dominated by riverine inputs rather than dust (according to the results of our geochemical end-member unmixing), with the inverse also true, particularly in ln[Zr/Rb]. Radiogenic Sr values may be attributed to enhanced chemical weathering under humid climates resulting in a higher proportion of fine clay minerals and micas reaching Site 659[42]. The covariation with unradiogenic ε_{Nd} values suggest there is also a shift in provenance, potentially attributable to transport of an increased proportion of proximal material sourced from the West African Craton transported by rivers compared to aeolian inputs, which may contain a greater contribution from the interior of the continent (or potentially Morocco, although the reported Sr isotope signatures[45] suggest this scenario is less likely).

Temporal variability in radiogenic isotope signatures

The radiogenic isotope signatures of the lithic fraction of the Site 659 sediments hint at subtle differences with sediment age, but we record no clear temporal shifts in the provenance of lithogenic material through the last 11 Myr to suggest major changes in the source regions of terrigenous sediment. The oldest samples (stage I) generally show more non-radiogenic isotope values in $^{87}Sr/^{86}Sr$ (Extended Data Figure 8c), which means that these Miocene-aged samples plot slightly closer to the Central source area than to the Western region, as defined by the currently available data[46] (Figure 4). Therefore, we infer that the strong signal of dust

inputs during stage I cannot be attributed to input from coastal sand dunes (which have previously been documented back to the Early Miocene and potentially much earlier[47,48]) and instead indicate the presence of strong dust generating regions in the continental interior back to at least the Late Miocene.

Fidelity of an astronomically-tuned age model at Site 659

Pronounced lithological and geochemical variability is well documented at Site 659, particularly over the younger intervals, and has been linked to astronomical forcing[2,19,49-51] (e.g. Figure 3, Supplementary Figure 6). These observations therefore provide an opportunity to capitalize on the potential to gain a high-fidelity age model for Site 659 by tuning the clear lithological cycles to an astronomical signal, as with many records of Mediterranean climate and low-latitude continental margins where a similar tuning approach has been used for chronology[52-56]. However, this approach requires care to ensure that age is assigned to our environmental records as independently as possible to guard against circularity. In our final age model, we used the core images and the ratio ln[Ca/Fe] to tune to insolation and [Al+Fe]/[Si+K+Ti] and ln[Zr/Rb] as our main records of environmental change.

To assess the extent to which astronomical power is present throughout the Site 659 records, we first analysed the frequencies present in our data using wavelet analysis[57] with an age model was based solely on bio- and magnetostratigraphic datums[15,58] and no tuning applied to the records (Extended Data Figure 5). The resulting continuous wavelet power spectrum show extremely similar patterns of variability on astronomical periodicities to our final, astronomically tuned record in both ln[Ca/Fe] and [Al+Fe]/[Si+K+Ti] across the full 11 Myr datasets (Extended Data Figure 5). This result indicates that the astronomical periodicities identified in the lithology and geochemistry of Site 659 sediments are genuine and have not been artificially tuned into the data. We also note that significant power is often detected concurrently at two or more frequencies, with the ratios between these frequencies matching those of major astronomical cycles (Extended Data Figures 5 and 6). This result would be very difficult to tune into our records artificially, providing further evidence for the lithological and geochemical variability at Site 659 being astronomically-paced.

Changing astronomical pacing of hydroclimate variability in North African over the past 11 Myr

To assess how the dominant frequencies of variability change throughout our >11 Myr records, we performed spectral analysis on our ln[Ca/Fe], [Al+Fe]/[Si+K+Ti] and dust flux data using REDFIT[59] to identify significant periodicities in our unevenly spaced data series (Extended Data Figure 6). Analyses were carried out using the PAST software[60]

REDFIT analysis reveals a strong signature of precession throughout the last 11 Myr in ln[Ca/Fe], [Al+Fe]/[Si+K+Ti] and dust flux data from Site 659 (Extended Data Figure 6), with obliquity also present in all three time intervals examined (stages I to III). Significant eccentricity is only recorded during stage I (>6.9 Ma), rather than the youngest 800 kyr when strong 100 kyr glacial cycles are recorded in benthic oxygen isotope records[61]. The signatures of obliquity and precession are seen in all three stages of our record, but are generally weakest in the oldest part of the record (stage I), likely, at least in part, because of the stronger smoothing effects of bioturbation where sedimentation rates are lower (Supplementary Figure 2).

The relative importance of high and low latitude forcing in driving African hydroclimate, particularly during the Quaternary Period, is debated[2,9,62-67]. The strong presence of precessional frequencies (23 and 19 kyr) in our data (Extended Data Figure 6) supports a major role for insolation forcing of the West African monsoon. Obliquity (41 kyr) is also

strongly present, which may indicate that the ice volume at high latitudes also exerts a major control on North African hydroclimate, perhaps by influencing wind strength. However, obliquity can also influence low latitude hydroclimate directly through modulation of the cross-equatorial insolation gradient[68]. The absence of an obvious strengthening of the obliquity signature associated with increasing amplitude of glacial-interglacial cycles in the Late Pliocene/early Pleistocene[61] in our hydroclimate proxy [Al+Fe]/[Si+K+Ti] (e.g. Extended Data Figure 5) supports this interpretation. The signal of obliquity in the latest Pliocene/Pleistocene appears slightly stronger in the ln[Ca/Fe] and dust flux records than [Al+Fe]/[Si+K+Ti] which may indicate the influence of glacial-interglacial shifts in overturning circulation bringing more corrosive bottom waters to the site driving carbonate dissolution[9] and/or higher latitude forcing exerting a stronger control over wind strength (and hence dust transport) than continental hydroclimate.

Interpreting plant wax history at Site 659

Long-chain *n*-alkanes originating from the epicuticular leaf waxes of terrestrial plants can be removed from the leaf surface by the action of wind or rain and transported to the ocean via both dust and rivers[69-71]. A strong correlation between concentrations of *n*-alkanes and dust percentages at Site 659 suggests that transport by wind is the dominant process at this location[2,19]. The source regions of plant waxes are likely very similar to those of the terrigenous material reaching Site 659, however, given the very low net primary production across much of North Africa, the plant wax signature may be biased to areas with higher biomass densities, particularly during arid time intervals.

Previous studies suggest that Site 659 records plant waxes dominantly sourced from the northern Sahel, with biomarker and pollen records suggesting a minor additional input of terrestrial material transported by the northeast trade winds from more northerly latitudes, evidenced during times of aridity and increased trade wind strength such as the Last Glacial Period, but not during the warmer and wetter Pliocene[18,19,72,73]. The Sahel is currently dominated by C_4 grasslands, while the vegetation in northernmost Africa is instead dominated by C_3 plants[74]. Therefore, the northwest African margin currently receives a mixture of plant waxes from these two sources. Several studies[72,75] estimate approximately equal proportions of inputs from C_4 and C_3 plants to recent and Late Quaternary aged marine sediments around the latitude of Site 659, however other, more recent studies point to a much higher contribution from C_4 plants[18,76].

Combined evidence from plant wax carbon isotopes and pollen indicates C_4 savanna grasslands directly replaced savannas dominated by C_3 grasses in both eastern and southern Africa as C_4 vegetation expanded through the Neogene[77,78]. Evidence of Poaceae (grasses) in the Niger delta as far back as the early Miocene[79] suggests a similar sequence of events unfolded in the Sahel, with a gradational increase in plant wax $\delta^{13}C$ of ca. 10 ‰ at Site 659 indicating an expansion of C_4 vegetation starting approximately 10 Myr ago[80]. Superimposed on this shift (at least during the Pliocene and Late Quaternary where high-resolution data exist) is variability in $\delta^{13}C$ driven by precession, obliquity and eccentricity[19]. These cycles have a typical magnitude of 0.5–2.5 ‰, much smaller than the multi-million year trend in plant wax $\delta^{13}C$ (Figure 2, Supplementary Figure 3).

We note that the relatively muted signature of astronomically-forced variability recorded at Site 659 is not observed at all locations across North Africa. Some localities record variability in plant wax $\delta^{13}C$ of >8 ‰ over astronomical timescales[81-86], most commonly records from lakes in East Africa where the topography can lead to diverse ecosystems in closer proximity to one another than further west. Lacustrine sediments also typically record larger variability in plant wax $\delta^{13}C$ than distal marine sediment cores[87] because lake archives document more

proximal vegetation sources, can be influenced by local tectonics and hydrography particularly in tectonically active regions such as East Africa, and may also be biased by microbially-derived *n*-alkanes[87]. Marine records integrate source material from across a large region and are less sensitive to subtle vegetation shifts than lake records although they can be influenced by transport processes[19,87].

A larger range of variability in *n*-alkane $\delta^{13}C$ in the Late Quaternary than Site 659 is also recorded at northwest African margin sites GeoB9508-5 (15.5°N, -21.2 to -26.5 ‰, ~65–100 % C_4)[76] and GeoB9528-3 (9.2°N, -21.8 to -28 ‰, ~55–100 % C_4)[88] (21.0°N, -23 to -25.7 ‰, ~70–90% C_4). Both GeoB9508-5 and GeoB9528-3 lie further south and closer to the continent than Site 659. Therefore, a scarcity of sources of waxes carrying very low carbon isotopic signatures in the Sahara due to a regional dominance of C_4 vegetation could be responsible for low amplitude variability in $\delta^{13}C$ at Site 659. That said, we note that the amplitude of astronomically-forced variability in *n*-alkane $\delta^{13}C$ at both GeoB9508-5 and GeoB9528-3 is only around half the magnitude of the multi-million year shift associated with C_4 grassland expansion. We also observe that the magnitude of astronomically-forced variability in $\delta^{13}C$ at Site 659 appears slightly smaller in the Pliocene than in the Last Glacial Cycle, despite lower $\delta^{13}C$ values indicating a greater proportion of C_3 plants in the older time period (Figure 2, Supplementary Figure 3). The *n*-alkane $\delta^{13}C$ data from the Late Miocene are not of sufficient resolution to assess the magnitude of astronomically-forced variability, however we do not observe an obvious relationship between $\delta^{13}C$ and our geochemical ratios to suggest that there was strong aridity-driven cyclicity at a time when isotopic signatures indicate significant inputs from both C_3 and C_4 plants.

In summary, we conclude that it is unlikely that the muted astronomically-forced variability in $\delta^{13}C$ recorded in both the Pliocene and Quaternary at Site 659 (compared to the high amplitude astronomically-forced changes in hydroclimate) can simply be explained by the absence of a C_3 plants in the regions of Northern Africa sampled by our records.

References for *p*CO_2 reconstructions

Badger et al. (2013)[89]
Badger et al. (2019)[90]
Bartoli et al. (2011)[91]
Bolton et al. (2016)[92]
Chalk et al. (2017)[93]
de la Vega et al. (2020)[94]
Dyez et al. (2018)[95]
Hönisch et al. (2009)[96]
Martinez-Boti et al. (2015)[97]
Pagani et al. (2005)[98]
Pagani et al. (2010)[99]
Seki et al. (2010)[100]
Sosdian et al. (2018)[101]
Stap et al. (2016)[102]
Super et al. (2018)[103]
Tanner et al. (2020)[104]
Zhang et al. (2013)[105]
Zhang et al. (2017)[106]
Zhang et al. (2019)[107]

Supplementary Figures

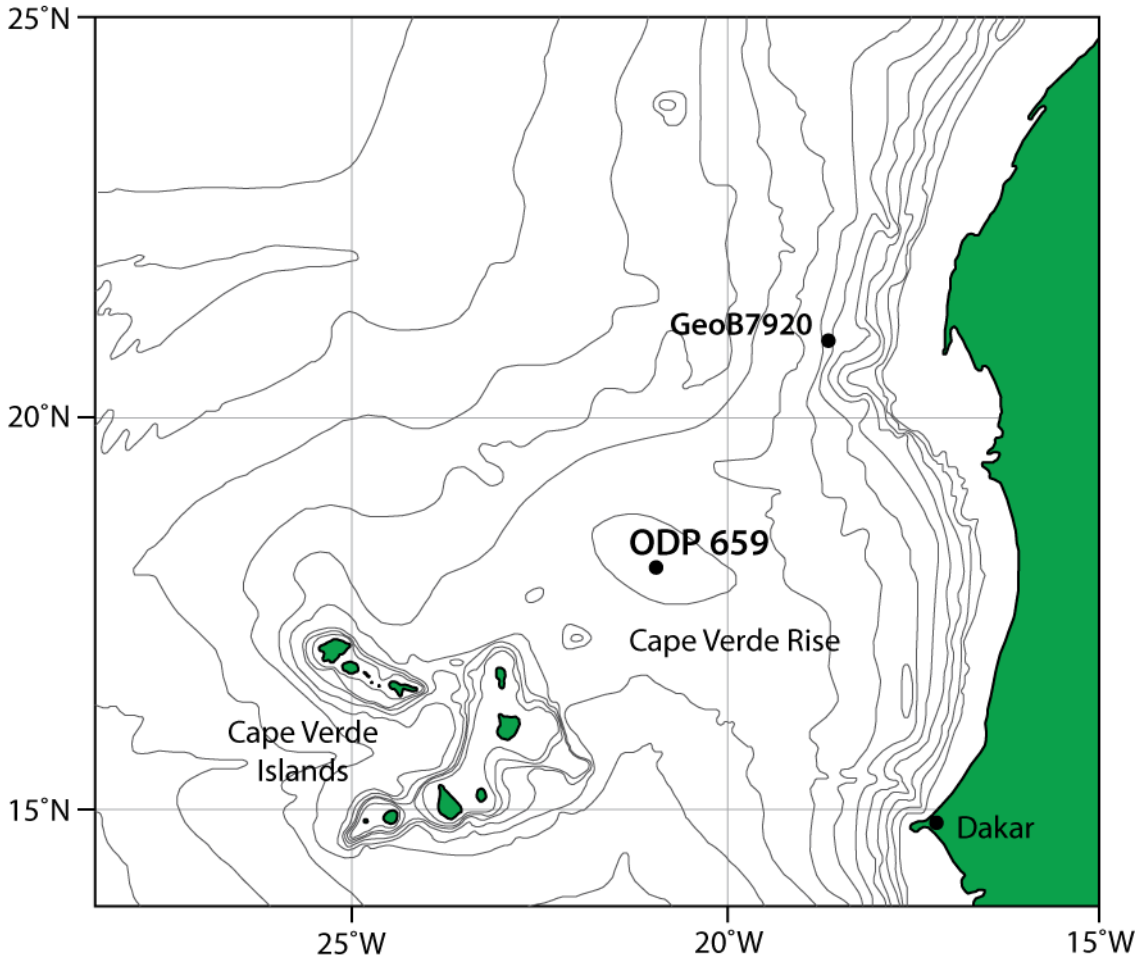

Supplementary Figure 1| Map indicating the location of ODP Site 659 and nearby site GeoB7920, offshore NW Africa. Site locations marked by black circles, adapted from Ruddiman et al. (1989)[15].

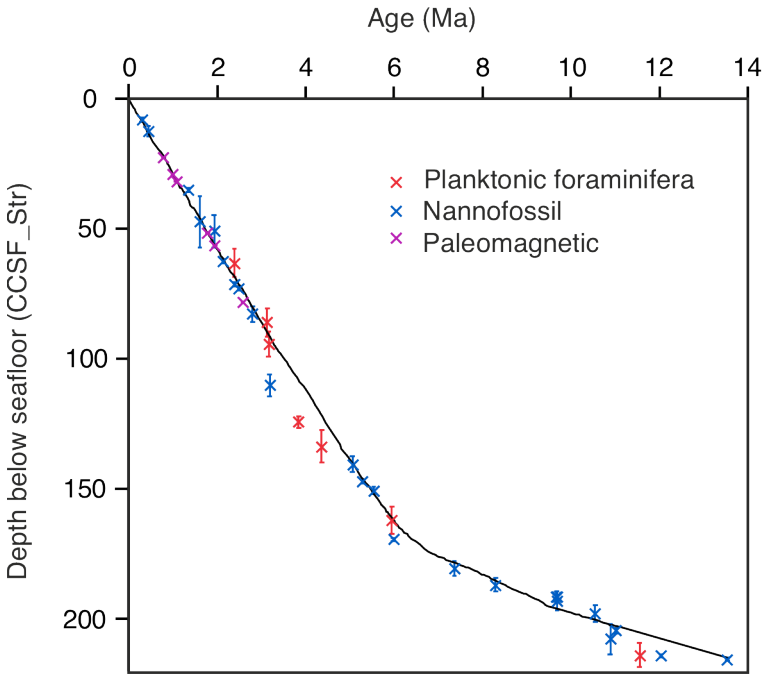

Supplementary Figure 2| Age depth plot for ODP Site 659. Age model created by benthic oxygen isotope correlation and orbital tuning used in this study (black line) compared to the original datums[58,108] (J. Backman pers. comm.), with depths converted onto the new splice and out-of-splice sections stretched to correlate to the splice where necessary using XRF data, bulk properties and core images. Biostratigraphic and magnetostratigraphic ages updated following Raffi et al. (2006)[109], Wade et al. (2011)[110] & Ogg (2012)[111]. Red crosses: planktonic foraminiferal datums, blue: nannofossil datums, purple: paleomagnetic reversals.

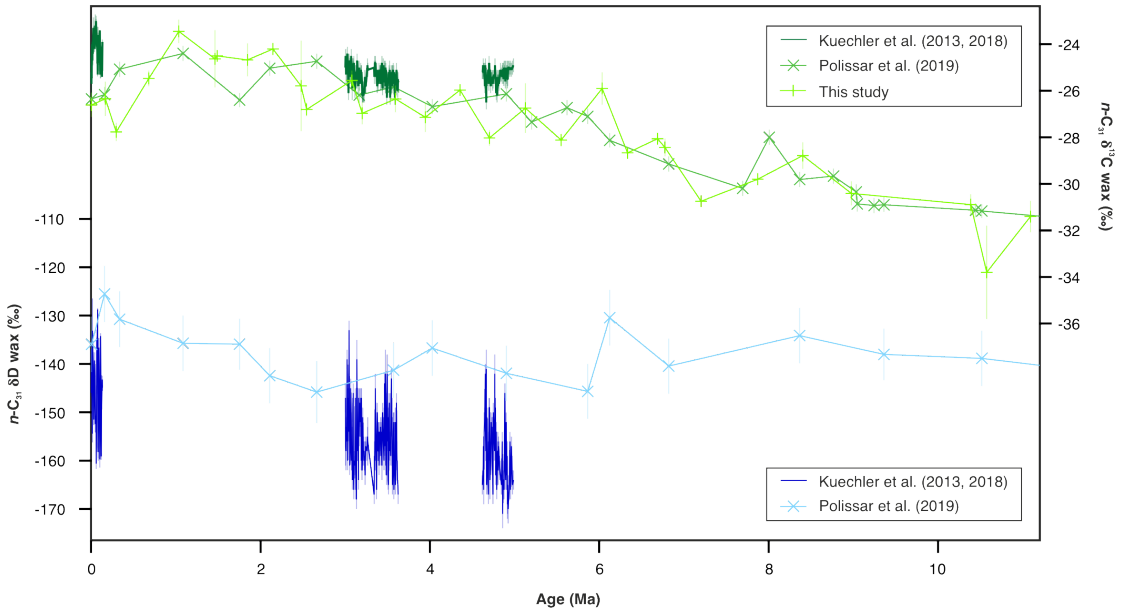

Supplementary Figure 3| Comparison of astronomically-forced variability and multi-million year trends in plant wax isotopes at Site 659. Top: $\delta^{13}C$ of C_{31} *n*-alkanes, data from Kuechler et al. (2013, 2018, line only)[18,19], Polissar et al (2019, crosses)[80] and this study (plusses). Bottom: δD of C_{31} *n*-alkanes, data from Kuechler et al. (2013, 2018, line only)[18,19] and Polissar et al (2019, crosses)[80]. Error bars indicate 1 s.e.m in the data of Polissar et al. (2019) and 1 sd in the data from both Kuechler et al. (2013, 2018) and this study.

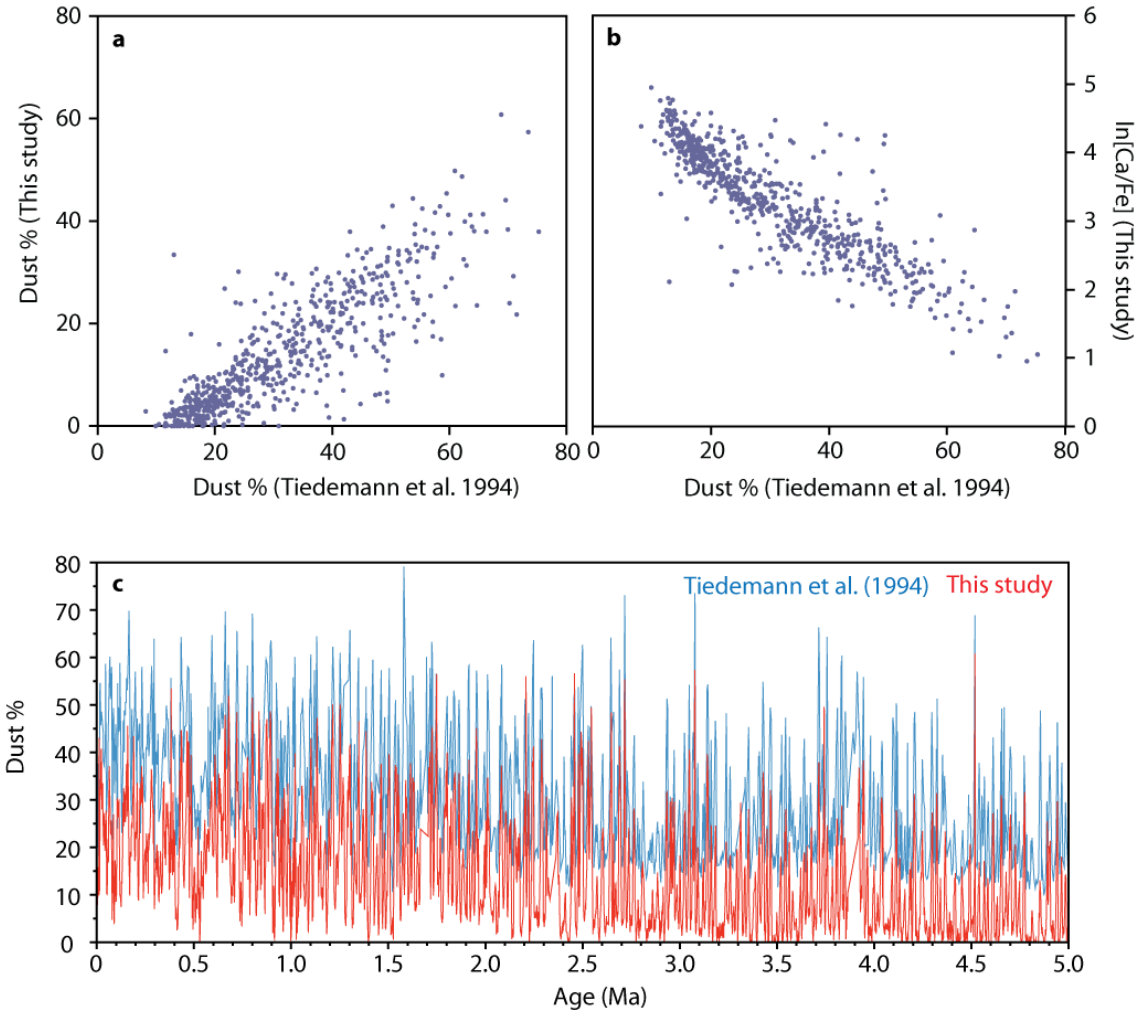

Supplementary Figure 4| Comparison of techniques for dust estimation at Site 659. Cross-plots of dust content as a percentage of the total sediment from Tiedemann et al. (1994)[2] plotted against: **a** % dust estimated by end-member unmixing (this study) and **b** ln[Ca/Fe] measured by XRF core scanning (this study). Measurements included in these plots were taken within 1 cm of each other. **c** Down core records of dust as a % of the total sediment by Tiedemann et al. 1994[2] (blue) and this study (red), from 0–5 Ma. All data have been converted onto the splice and age model developed in this study.

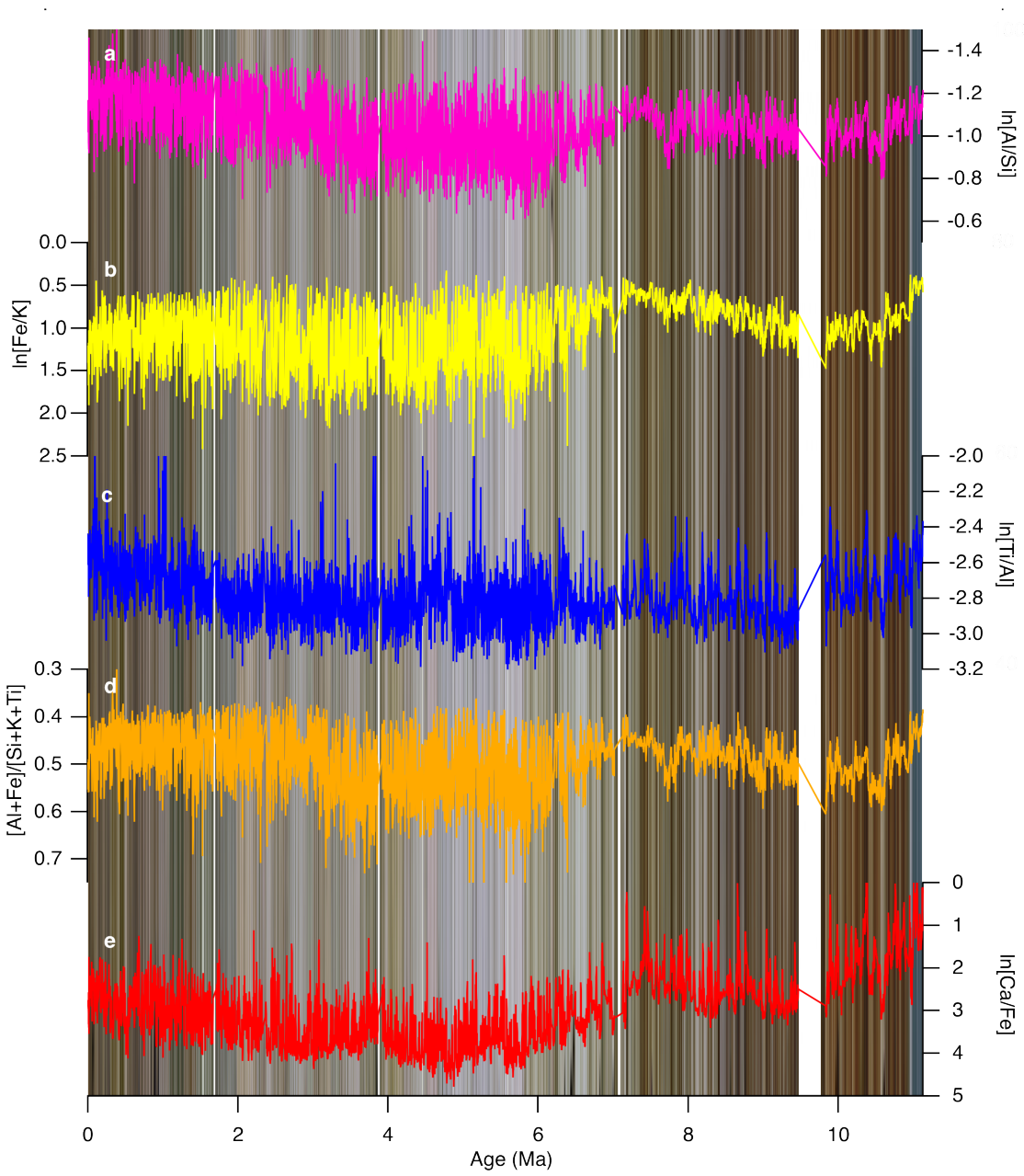

Supplementary Figure 5| Comparison of calibrated XRF ratios of Site 659 sediments spanning 0–11.2 Ma. **a** ln[Al/Si], **b** ln[Fe/K], **c** ln[Ti/Al], **d** [Al+Fe]/[Si+K+Ti], **e** ln[Ca/Fe]. Background image is a composited core photograph.

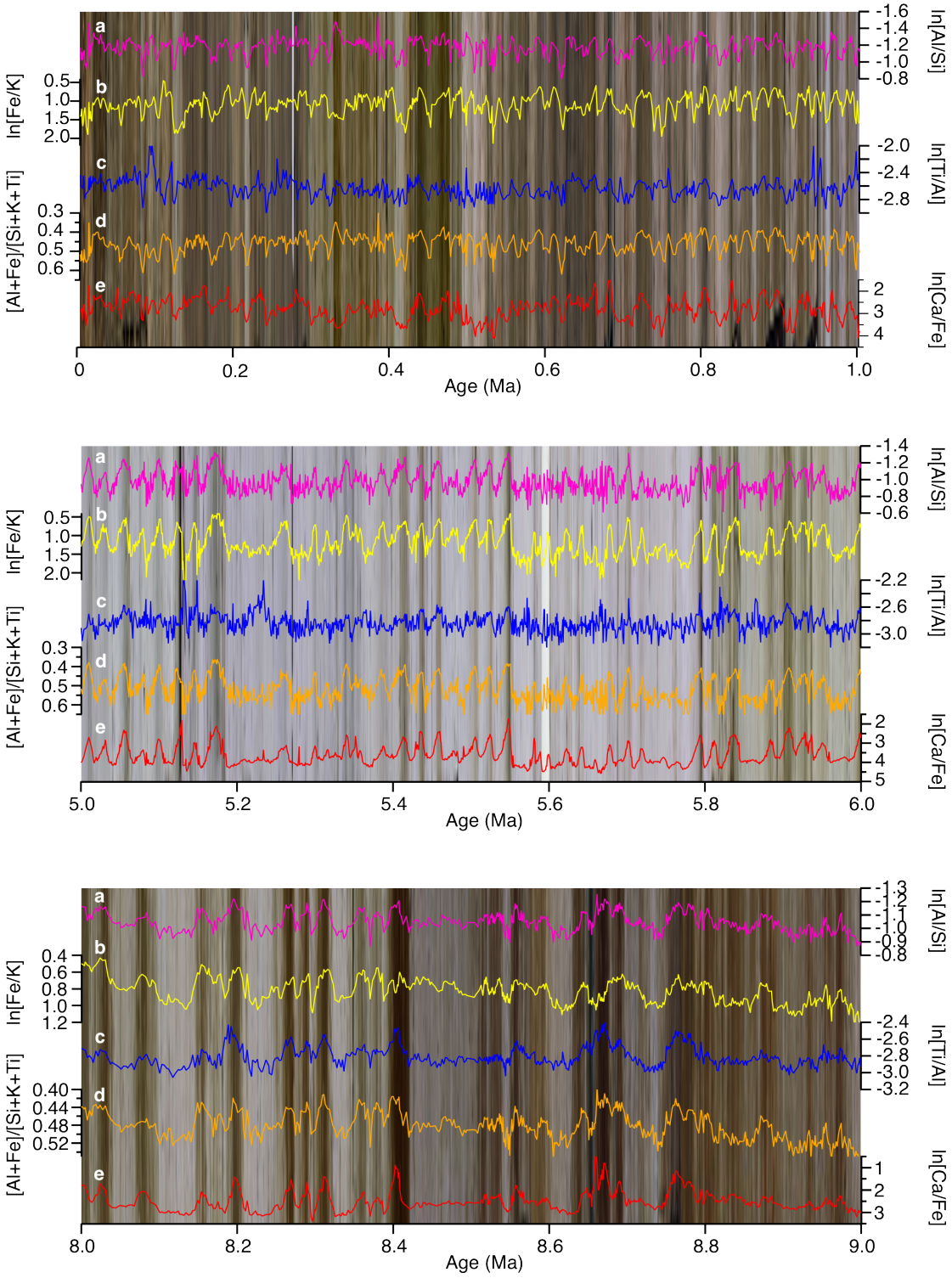

Supplementary Figure 6| Comparison of snapshots of calibrated XRF ratios of Site 659 sediment, with an example from each of zone I–III. Top: 0–1 Ma, middle 5–6 Ma, bottom 8–9 Ma. **a** ln[Al/Si], **b** ln[Fe/K], **c** ln[Ti/Al], **d** [Al+Fe]/[Si+K+Ti], **e** ln[Ca/Fe]. Background images are composited core photographs.

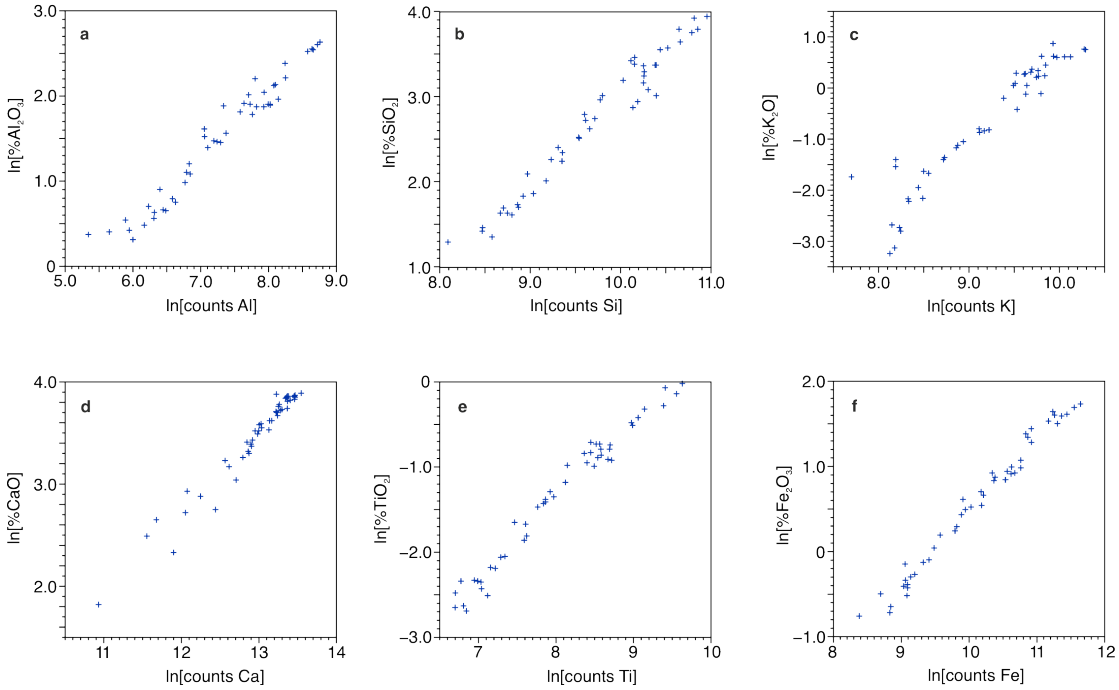

Supplementary Figure 7| Comparison of measurements of major element abundances in the calibration sample set between Avaatech XRF core scanner counts and oxide concentrations measured by discrete sample XRF analysis. **a** Al, **b** Si, **c** K, **d** Ca, **e** Ti and **f** Fe.

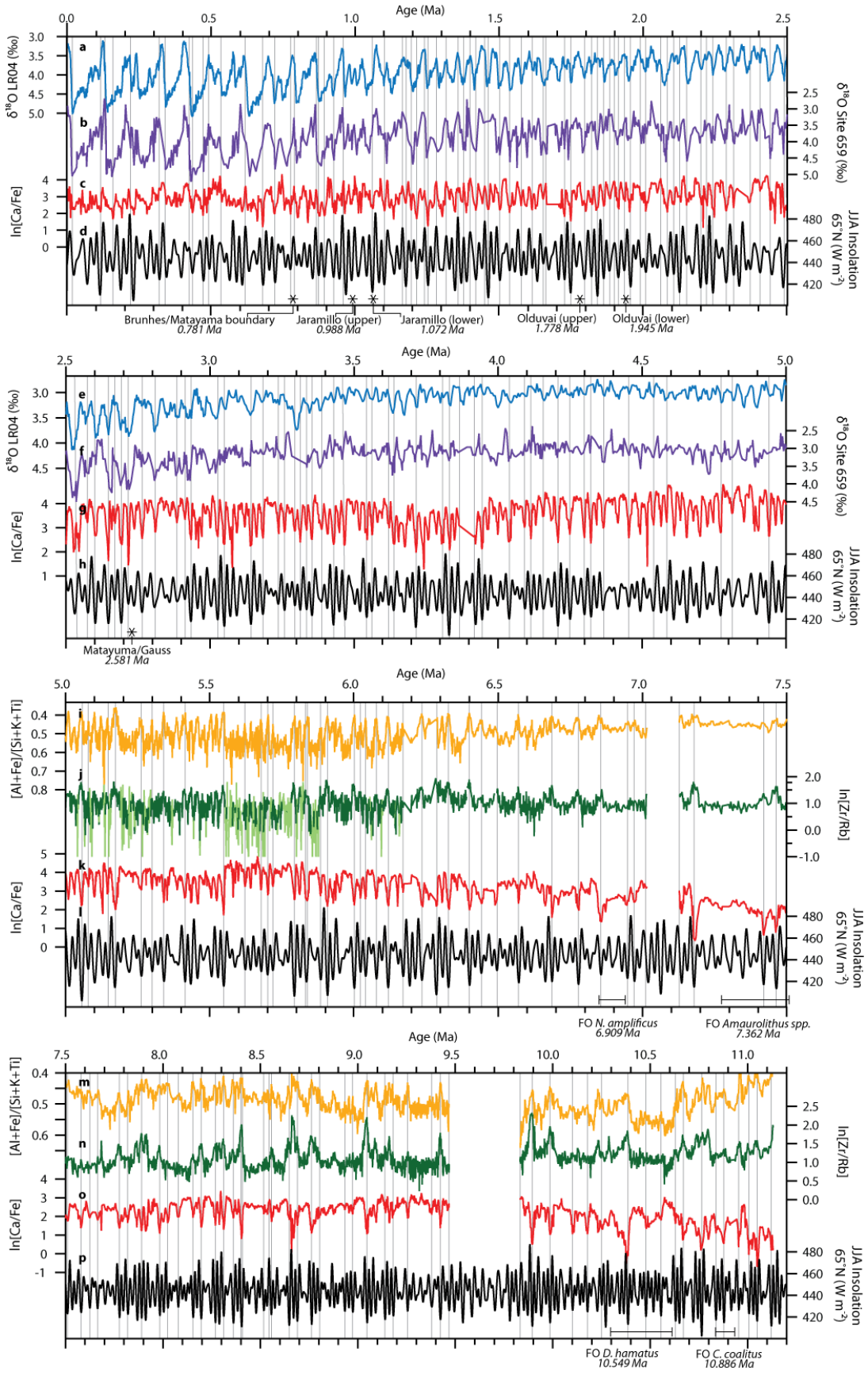

Supplementary Figure 8| Stratigraphic tie-points used in the construction of the Site 659 age model. **a,e** LR04 benthic foraminiferal oxygen isotope stack[61]. **b,f** Site 659 *C. wullerstorfi* oxygen isotope values[2] converted onto on our new composite depth scale and age model. **c,g,k,o** Calibrated ln[Ca/Fe] values of Site 659 sediments. **d,h,l,p** Mean boreal summer insolation (June-August) at 65°N given by the La2004 orbital solution[112]. **i,m** Calibrated

[Al+Fe]/[Si+K+Ti] ratios of Site 659 bulk sediment. **j,n** ln[Zr/Rb] values of Site 659 sediments (pale colour indicates low counts). Grey vertical lines mark the position of tie points used to generate the age model. The position of magnetostratigraphic boundaries as identified in the Leg 108 Scientific Results[108] are marked by stars, with listed ages from the Geologic Time Scale 2012 (GTS2012)[111], and biostratigraphic events (as identified in the Leg 108 Scientific Results[58] and J. Backman pers. comm.) are marked by bars, with ages updated following Raffi et al. (2006)[109]. Magnetostratigraphic and biostratigraphic dates were used to guide tuning.

References for Supplementary Information

1 Tiedemann, R., Sarnthein, M. & Stein, R. in *Proceedings of the Ocean Drilling Program, Scientific Results*. Vol. 108, 241-277 (ODP, 1989).

2 Tiedemann, R., Sarnthein, M. & Shackleton, N. J. Astronomic timescale for the Pliocene Atlantic δ18O and dust flux records of Ocean Drilling Program Site 659. *Paleoceanography* **9**, 619-638 (1994).

3 Ólafsdóttir, K. B., Schulz, M. & Mudelsee, M. REDFIT-X: Cross-spectral analysis of unevenly spaced paleoclimate time series. *Computers & Geosciences* **91**, 11-18 (2016).

4 Tjallingii, R. *et al.* Coherent high- and low-latitude control of the northwest African hydrological balance. *Nature Geosci* **1**, 670-675 (2008).

5 Skonieczny, C. *et al.* African humid periods triggered the reactivation of a large river system in Western Sahara. *Nat Commun* **6,** 8751 (2015).

6 Francois, R., Frank, M., Rutgers van der Loeff, M. M. & Bacon, M. P. 230Th normalization: An essential tool for interpreting sedimentary fluxes during the late Quaternary. *Paleoceanography* **19** (2004).

7 Adkins, J., deMenocal, P. & Eshel, G. The "African humid period" and the record of marine upwelling from excess 230Th in Ocean Drilling Program Hole 658C. *Paleoceanography* **21**, PA4203 (2006).

8 McGee, D., deMenocal, P. B., Winckler, G., Stuut, J. B. W. & Bradtmiller, L. I. The magnitude, timing and abruptness of changes in North African dust deposition over the last 20,000 yr. *Earth and Planetary Science Letters* **371-372**, 163-176 (2013).

9 Skonieczny, C. *et al.* Monsoon-driven Saharan dust variability over the past 240,000 years. *Science Advances* **5**, eaav1887 (2019).

10 Kinsley, C. W. *et al.* Orbital- and Millennial-Scale Variability in Northwest African Dust Emissions Over the Past 67,000 years. *Paleoceanography and Paleoclimatology* **36**, e2020PA004137 (2022).

11 Wood, S. N. *Generalized additive models: an introduction with R*. (CRC press, 2017).

12 R: A language and environment for statistical computing. https://www.R-project.org/ (Vienna, Austria, 2020).

13 Govin, A. *et al.* Distribution of major elements in Atlantic surface sediments (36°N–49°S): Imprint of terrigenous input and continental weathering. *Geochemistry, Geophysics, Geosystems* **13**, Q01013 (2012).

14 Meckler, A. N. *et al.* Deglacial pulses of deep-ocean silicate into the subtropical North Atlantic Ocean. *Nature* **495**, 495-498 (2013).

15 Ruddiman, W. F., Sarnthein, M., Baldauf, J. G. & et al. *Proc. ODP, Init. Repts., 108*. (ODP, 1989).

16 Tjallingii, R. *Application and quality of X-ray fluorescence core scanning in reconstructing late Pleistocene NW African continental margin sedimentation patterns and paleoclimate variations* PhD thesis, University of Bremen, (2006).

17 Sachse, D. *et al.* Molecular Paleohydrology: Interpreting the Hydrogen-Isotopic Composition of Lipid Biomarkers from Photosynthesizing Organisms. *Annual Review of Earth and Planetary Sciences* **40**, 221-249 (2012).

18 Kuechler, R. R., Schefuß, E., Beckmann, B., Dupont, L. & Wefer, G. NW African hydrology and vegetation during the Last Glacial cycle reflected in plant-wax-specific hydrogen and carbon isotopes. *Quaternary Science Reviews* **82**, 56-67 (2013).

19 Kuechler, R. R., Dupont, L. M. & Schefuß, E. Hybrid insolation forcing of Pliocene monsoon dynamics in West Africa. *Climate of the Past* **14**, 73-84 (2018).

20 Wilkens, R. H. *et al.* Revisiting the Ceara Rise, equatorial Atlantic Ocean: isotope stratigraphy of ODP Leg 154 from 0 to 5 Ma. *Clim. Past* **13**, 779-793 (2017).

21 Trauth, M. H., Larrasoaña, J. C. & Mudelsee, M. Trends, rhythms and events in Plio-Pleistocene African climate. *Quaternary Science Reviews* **28**, 399-411 (2009).

22 Stuut, J.-B. *et al.* Provenance of present-day eolian dust collected off NW Africa. *Journal of Geophysical Research: Atmospheres* **110**, D04202 (2005).

23 Reid, J. S. *et al.* Comparison of size and morphological measurements of coarse mode dust particles from Africa. *Journal of Geophysical Research: Atmospheres* **108(D19)**, 8593 (2003).

24 Arimoto, R., Ray, B. J., Lewis, N. F., Tomza, U. & Duce, R. A. Mass-particle size distributions of atmospheric dust and the dry deposition of dust to the remote ocean. *Journal of Geophysical Research: Atmospheres* **102**, 15867-15874 (1997).

25 Maher, B. A. *et al.* Global connections between aeolian dust, climate and ocean biogeochemistry at the present day and at the last glacial maximum. *Earth-Science Reviews* **99**, 61-97 (2010).

26 Rea, D. K. The paleoclimatic record provided by eolian deposition in the deep sea: The geologic history of wind. *Reviews of Geophysics* **32**, 159-195 (1994).

27 Friese, C. A. *et al.* Environmental factors controlling the seasonal variability in particle size distribution of modern Saharan dust deposited off Cape Blanc. *Aeolian Research* **22**, 165-179 (2016).

28 van der Does, M., Pourmand, A., Sharifi, A. & Stuut, J.-B. W. North African mineral dust across the tropical Atlantic Ocean: Insights from dust particle size, radiogenic Sr-Nd-Hf isotopes and rare earth elements (REE). *Aeolian Research* **33**, 106-116 (2018).
29 van der Does, M., Korte, L. F., Munday, C. I., Brummer, G.-J. A. & Stuut, J.-B. W. Particle size traces modern Saharan dust transport and deposition across the equatorial North Atlantic. *Atmospheric Chemistry and Physics* **16**, 13697 (2016).
30 Holz, C., Stuut, J.-B. W. & Henrich, R. Terrigenous sedimentation processes along the continental margin off NW Africa: implications from grain-size analysis of seabed sediments. *Sedimentology* **51**, 1145-1154 (2004).
31 Drake, N. A., Blench, R. M., Armitage, S. J., Bristow, C. S. & White, K. H. Ancient watercourses and biogeography of the Sahara explain the peopling of the desert. *Proceedings of the National Academy of Sciences* **108**, 458-462 (2011).
32 Krastel, S. *et al.* CapTimiris Canyon: A newly discovered channel system offshore of Mauritania. *Eos, Transactions American Geophysical Union* **85**, 417-423 (2004).
33 Zühlsdorff, C., Wien, K., Stuut, J. B. W. & Henrich, R. Late Quaternary sedimentation within a submarine channel–levee system offshore Cap Timiris, Mauritania. *Marine Geology* **240**, 217-234 (2007).
34 Holz, C., Stuut, J.-B. W., Henrich, R. d. & Meggers, H. Variability in terrigenous sedimentation processes off northwest Africa and its relation to climate changes: Inferences from grain-size distributions of a Holocene marine sediment record. *Sedimentary Geology* **202**, 499-508 (2007).
35 Grousset, F. E. *et al.* Saharan wind regimes traced by the Sr–Nd isotopic composition of subtropical composition of subtropical Atlantic sediments: Last Glacial Maximum vs today. *Quaternary Science Reviews* **17**, 395-409 (1998).
36 McCave, I. N. Particulate size spectra, behavior, and origin of nepheloid layers over the Nova Scotian Continental Rise. *Journal of Geophysical Research: Oceans* **88**, 7647-7666 (1983).
37 Gardner, W. D., Richardson, M. J. & Mishonov, A. V. Global assessment of benthic nepheloid layers and linkage with upper ocean dynamics. *Earth and Planetary Science Letters* **482**, 126-134 (2018).
38 Biscaye, P. E. & Eittreim, S. L. Suspended particulate loads and transports in the nepheloid layer of the abyssal Atlantic Ocean. *Marine Geology* **23**, 155-172 (1977).
39 Mulitza, S. *et al.* Increase in African dust flux at the onset of commercial agriculture in the Sahel region. *Nature* **466**, 226-228 (2010).
40 Castillo, S. *et al.* Trace element variation in size-fractionated African desert dusts. *Journal of Arid Environments* **72**, 1034-1045 (2008).
41 Skonieczny, C. *et al.* A three-year time series of mineral dust deposits on the West African margin: Sedimentological and geochemical signatures and implications for interpretation of marine paleo-dust records. *Earth and Planetary Science Letters* **364**, 145-156 (2013).
42 Meyer, I., Davies, G. R. & Stuut, J.-B. Grain size control on Sr-Nd isotope provenance studies and impact on paleoclimate reconstructions: An example from deep-sea sediments offshore NW Africa. *Geochemistry, Geophysics, Geosystems* **12**, Q03005 (2011).
43 Dasch, E. J. Strontium isotopes in weathering profiles, deep-sea sediments, and sedimentary rocks. *Geochimica et Cosmochimica Acta* **33**, 1521-1552 (1969).
44 Aarons, S. M., Aciego, S. M. & Gleason, J. D. Variable HfSrNd radiogenic isotopic compositions in a Saharan dust storm over the Atlantic: Implications for dust flux to oceans, ice sheets and the terrestrial biosphere. *Chemical Geology* **349-350**, 18-26 (2013).
45 Zhao, W., Balsam, W., Williams, E., Long, X. & Ji, J. Sr–Nd–Hf isotopic fingerprinting of transatlantic dust derived from North Africa. *Earth and Planetary Science Letters* **486**, 23-31 (2018).
46 Jewell, A. M. *et al.* Three North African dust source areas and their geochemical fingerprint. *Earth and Planetary Science Letters* **554**, 116645 (2021).
47 Sarnthein, M. *et al.* in *Geology of the Northwest African Continental Margin* (eds Ulrich von Rad, Karl Hinz, Michael Sarnthein, & Eugen Seibold) 545-604 (Springer Berlin Heidelberg, 1982).
48 Lever, A. & McCave, I. N. Eolian components in Cretaceous and Tertiary North Atlantic sediments. *Journal of Sedimentary Research* **53**, 811-832 (1983).
49 Colin, C. *et al.* Late Miocene to early Pliocene climate variability off NW Africa (ODP 659). *Palaeogeography, Palaeoclimatology, Palaeoecology* **401**, 81-95 (2014).
50 Vallé, F., Dupont, L. M., Leroy, S. A. G., Schefuß, E. & Wefer, G. Pliocene environmental change in West Africa and the onset of strong NE trade winds (ODP Sites 659 and 658). *Palaeogeography, Palaeoclimatology, Palaeoecology* **414**, 403-414 (2014).
51 Ruddiman, W. F. *et al.* in *Proceedings of the Ocean Drilling Program: Scientific Results*. Vol. 108 (ODP, 1989).
52 Zeeden, C. *et al.* Revised Miocene splice, astronomical tuning and calcareous plankton biochronology of ODP Site 926 between 5 and 14.4 Ma. *Palaeogeography, Palaeoclimatology, Palaeoecology* **369**, 430-451 (2013).

53 Krijgsman, W., Hilgen, F. J., Raffi, I., Sierro, F. J. & Wilson, D. S. Chronology, causes and progression of the Messinian salinity crisis. *Nature* **400**, 652-655 (1999).
54 Mourik, A. A. *et al.* Astronomical tuning of the La Vedova High Cliff section (Ancona, Italy) – Implications of the Middle Miocene Climate Transition for Mediterranean sapropel formation. *Earth and Planetary Science Letters* **297**, 249-261 (2010).
55 Krijgsman, W., Fortuin, A. R., Hilgen, F. J. & Sierro, F. J. Astrochronology for the Messinian Sorbas basin (SE Spain) and orbital (precessional) forcing for evaporite cyclicity. *Sedimentary Geology* **140**, 43-60 (2001).
56 van der Laan, E. *et al.* Astronomical forcing of Northwest African climate and glacial history during the late Messinian (6.5–5.5 Ma). *Palaeogeography, Palaeoclimatology, Palaeoecology* **313–314**, 107-126 (2012).
57 Grinsted, A., Moore, J. C. & Jevrejeva, S. Application of the cross wavelet transform and wavelet coherence to geophysical time series. *Nonlinear processes in geophysics* **11**, 561-566 (2004).
58 Manivit, H. in *Proceedings of the Ocean Drilling Program, Scientific Results, Vol.108* (ed W. Ruddiman, Sarnthein, M., et al.,) 35-69 (ODP, 1989).
59 Schulz, M. & Mudelsee, M. REDFIT: estimating red-noise spectra directly from unevenly spaced paleoclimatic time series. *Computers & Geosciences* **28**, 421-426 (2002).
60 Hammer, Ø., Harper, D. A. T. & Ryan, P. D. PAST: Paleontological Statistics Software Package for Education and Data Analysis. *Palaeontologia Electronica* **4**, 9 (2001).
61 Lisiecki, L. E. & Raymo, M. E. A Pliocene-Pleistocene stack of 57 globally distributed benthic δ18O records. *Paleoceanography* **20**, PA1003 (2005).
62 Tierney, J. E., deMenocal, P. B. & Zander, P. D. A climatic context for the out-of-Africa migration. *Geology* **45**, 1023-1026 (2017).
63 deMenocal, P. B., Ruddiman, W. F. & Pokras, E. M. Influences of High- and Low-Latitude Processes on African Terrestrial Climate: Pleistocene Eolian Records from Equatorial Atlantic Ocean Drilling Program Site 663. *Paleoceanography* **8**, 209-242 (1993).
64 Pokras, E. M. & Mix, A. C. Earth's precession cycle and Quaternary climatic change in tropical Africa. *Nature* **326**, 486-487 (1987).
65 Larrasoaña, J. C., Roberts, A. P., Rohling, E. J., Winklhofer, M. & Wehausen, R. Three million years of monsoon variability over the northern Sahara. *Climate Dynamics* **21**, 689-698 (2003).
66 de Boer, B., Peters, M. & Lourens, L. J. The transient impact of the African monsoon on Plio-Pleistocene Mediterranean sediments. *Clim. Past* **17**, 331-344 (2021).
67 Kutzbach, J. E. *et al.* African climate response to orbital and glacial forcing in 140,000-y simulation with implications for early modern human environments. *Proceedings of the National Academy of Sciences*, **117 (5)**, 2255-2264 (2020).
68 Bosmans, J. H. C., Hilgen, F. J., Tuenter, E. & Lourens, L. J. Obliquity forcing of low-latitude climate. *Clim. Past* **11**, 1335-1346 (2015).
69 Schefuß, E., Ratmeyer, V., Stuut, J.-B. W., Jansen, J. H. F. & Sinninghe Damsté, J. S. Carbon isotope analyses of n-alkanes in dust from the lower atmosphere over the central eastern Atlantic. *Geochimica et Cosmochimica Acta* **67**, 1757-1767 (2003).
70 Eglinton, T. I. & Eglinton, G. Molecular proxies for paleoclimatology. *Earth and Planetary Science Letters* **275**, 1-16 (2008).
71 Rommerskirchen, F. *et al.* A north to south transect of Holocene southeast Atlantic continental margin sediments: Relationship between aerosol transport and compound-specific δ13C land plant biomarker and pollen records. *Geochemistry, Geophysics, Geosystems* **4** (2003).
72 Zhao, M., Dupont, L., Eglinton, G. & Teece, M. n-Alkane and pollen reconstruction of terrestrial climate and vegetation for N.W. Africa over the last 160 kyr. *Organic Geochemistry* **34**, 131-143 (2003).
73 Hooghiemstra, H., Bechler, A. & Beug, H.-J. Isopollen maps for 18,000 years B.P. of the Atlantic offshore of northwest Africa: Evidence for paleowind circulation. *Paleoceanography* **2**, 561-582 (1987).
74 Ehleringer, J. R. & Cerling, T. E. in *Global Biogeochemical Cycles in the Climate System* (eds Ernst-Detlef Schulze *et al.*) 267-277 (Academic Press, 2001).
75 Huang, Y., Dupont, L., Sarnthein, M., Hayes, J. M. & Eglinton, G. Mapping of C4 plant input from North West Africa into North East Atlantic sediments. *Geochimica et Cosmochimica Acta* **64**, 3505-3513 (2000).
76 Niedermeyer, E. M. *et al.* Orbital- and millennial-scale changes in the hydrologic cycle and vegetation in the western African Sahel: insights from individual plant wax δD and δ13C. *Quaternary Science Reviews* **29**, 2996-3005 (2010).
77 Hoetzel, S., Dupont, L., Schefusz, E., Rommerskirchen, F. & Wefer, G. The role of fire in Miocene to Pliocene C4 grassland and ecosystem evolution. *Nature Geosci* **6**, 1027-1030 (2013).
78 Feakins, S. J. *et al.* Northeast African vegetation change over 12 m.y. *Geology* **41** (3), 295–298 (2013).
79 Morley, R. J. & Richards, K. Gramineae cuticle: a key indicator of Late Cenozoic climatic change in the Niger Delta. *Review of Palaeobotany and Palynology* **77**, 119-127 (1993).

80 Polissar, P. J., Rose, C., Uno, K. T., Phelps, S. R. & deMenocal, P. Synchronous rise of African C4 ecosystems 10 million years ago in the absence of aridification. *Nature Geoscience* **12**, 657-660 (2019).
81 Tierney, J. E., Russell, J. M. & Huang, Y. A molecular perspective on Late Quaternary climate and vegetation change in the Lake Tanganyika basin, East Africa. *Quaternary Science Reviews* **29**, 787-800 (2010).
82 Beuning, K. R. M., Talbot, M. R., Livingstone, D. A. & Schmukler, G. Sensitivity of carbon isotopic proxies to paleoclimatic forcing: A case study from Lake Bosumtwi, Ghana, over the last 32,000 years. *Global Biogeochemical Cycles* **17,** 1121 (2003).
83 Sinninghe Damsté, J. S. *et al.* A 25,000-year record of climate-induced changes in lowland vegetation of eastern equatorial Africa revealed by the stable carbon-isotopic composition of fossil plant leaf waxes. *Earth and Planetary Science Letters* **302**, 236-246 (2011).
84 Lupien, R. L. *et al.* Vegetation change in the Baringo Basin, East Africa across the onset of Northern Hemisphere glaciation 3.3–2.6 Ma. *Palaeogeography, Palaeoclimatology, Palaeoecology* **570**, 109426 (2021).
85 Lupien, R. L. *et al.* A leaf wax biomarker record of early Pleistocene hydroclimate from West Turkana, Kenya. *Quaternary Science Reviews* **186**, 225-235 (2018).
86 Tierney, J. E. & deMenocal, P. B. Abrupt Shifts in Horn of Africa Hydroclimate Since the Last Glacial Maximum. *Science* **342**, 843-846 (2013).
87 Feakins, S. J., Eglinton, T. I. & deMenocal, P. B. A comparison of biomarker records of northeast African vegetation from lacustrine and marine sediments (ca. 3.40 Ma). *Organic Geochemistry* **38**, 1607-1624 (2007).
88 Castañeda, I. S. *et al.* Wet phases in the Sahara/Sahel region and human migration patterns in North Africa. *Proceedings of the National Academy of Sciences* **106**, 20159-20163 (2009).
89 Badger, M. P. S. *et al.* CO2 drawdown following the middle Miocene expansion of the Antarctic Ice Sheet. *Paleoceanography* **28**, 42-53 (2013).
90 Badger, M. P. S. *et al.* Insensitivity of alkenone carbon isotopes to atmospheric CO2 at low to moderate CO2 levels. *Clim. Past* **15**, 539-554 (2019).
91 Bartoli, G., Hönisch, B. & Zeebe, R. E. Atmospheric CO2 decline during the Pliocene intensification of Northern Hemisphere glaciations. *Paleoceanography* **26**, PA4213 (2011).
92 Bolton, C. T. *et al.* Decrease in coccolithophore calcification and CO2 since the middle Miocene. *Nat Commun* **7**, 10284 (2016).
93 Chalk, T. B. *et al.* Causes of ice age intensification across the Mid-Pleistocene Transition. *Proceedings of the National Academy of Sciences* **114**, 13114 (2017).
94 de la Vega, E., Chalk, T. B., Wilson, P. A., Bysani, R. P. & Foster, G. L. Atmospheric CO2 during the Mid-Piacenzian Warm Period and the M2 glaciation. *Scientific Reports* **10**, 11002 (2020).
95 Dyez, K. A., Hönisch, B. & Schmidt, G. A. Early Pleistocene Obliquity-Scale pCO2 Variability at ~1.5 Million Years Ago. *Paleoceanography and Paleoclimatology* **33**, 1270-1291 (2018).
96 Hönisch, B., Hemming, N. G., Archer, D., Siddall, M. & McManus, J. F. Atmospheric Carbon Dioxide Concentration Across the Mid-Pleistocene Transition. *Science* **324**, 1551-1554 (2009).
97 Martinez-Boti, M. A. *et al.* Plio-Pleistocene climate sensitivity evaluated using high-resolution CO2 records. *Nature* **518**, 49-54 (2015).
98 Pagani, M., Zachos, J. C., Freeman, K. H., Tipple, B. & Bohaty, S. Marked Decline in Atmospheric Carbon Dioxide Concentrations During the Paleogene. *Science* **309**, 600-603 (2005).
99 Pagani, M., Liu, Z., LaRiviere, J. & Ravelo, A. C. High Earth-system climate sensitivity determined from Pliocene carbon dioxide concentrations. *Nature Geoscience* **3**, 27 (2010).
100 Seki, O. *et al.* Alkenone and boron-based Pliocene pCO2 records. *Earth and Planetary Science Letters* **292**, 201-211 (2010).
101 Sosdian, S. M. *et al.* Constraining the evolution of Neogene ocean carbonate chemistry using the boron isotope pH proxy. *Earth and Planetary Science Letters* **498**, 362-376 (2018).
102 Stap, L. B. *et al.* CO2 over the past 5 million years: Continuous simulation and new δ11B-based proxy data. *Earth and Planetary Science Letters* **439**, 1-10 (2016).
103 Super, J. R. *et al.* North Atlantic temperature and pCO2 coupling in the early-middle Miocene. *Geology* **46**, 519-522 (2018).
104 Tanner, T., Hernández-Almeida, I., Drury, A. J., Guitián, J. & Stoll, H. Decreasing Atmospheric CO2 During the Late Miocene Cooling. *Paleoceanography and Paleoclimatology* **35**, e2020PA003925 (2020).
105 Zhang, Y. G., Pagani, M., Liu, Z., Bohaty, S. M. & DeConto, R. A 40-million-year history of atmospheric CO2. *Philosophical Transactions of the Royal Society of London A: Mathematical, Physical and Engineering Sciences* **371**, 20130096 (2013).
106 Zhang, Y. G., Pagani, M., Henderiks, J. & Ren, H. A long history of equatorial deep-water upwelling in the Pacific Ocean. *Earth and Planetary Science Letters* **467**, 1-9 (2017).
107 Zhang, Y. G. *et al.* Refining the alkenone-pCO2 method I: Lessons from the Quaternary glacial cycles. *Geochimica et Cosmochimica Acta* **260**, 177-191 (2019).

108 Tauxe, L., Valet, J.-P. & Bloemendal, J. in *Proc. ODP, Sci. Results, 108* (ed W. Ruddiman, Sarnthein, M., et al.,) 429–439 (ODP, 1989).
109 Raffi, I. *et al.* A review of calcareous nannofossil astrobiochronology encompassing the past 25 million years. *Quaternary Science Reviews* **25**, 3113-3137 (2006).
110 Wade, B. S., Pearson, P. N., Berggren, W. A. & Pälike, H. Review and revision of Cenozoic tropical planktonic foraminiferal biostratigraphy and calibration to the geomagnetic polarity and astronomical time scale. *Earth-Science Reviews* **104**, 111-142 (2011).
111 Ogg, J. G. in *The Geologic Time Scale* (eds Felix M. Gradstein, James G. Ogg, Mark D. Schmitz, & Gabi M. Ogg) 85-113 (Elsevier, 2012).
112 Laskar, J. *et al.* A long-term numerical solution for the insolation quantities of the Earth. *Astronomy & Astrophysics* **428**, 261-285 (2004).